*J. Fluid Mech.* (2005), *vol.* 537, *pp.* 317–347.  
doi:10.1017/S0022112005005227 Printed in the United Kingdom

# Analysis of weakly turbulent dilute-spray flames and spray combustion regimes

By JULIEN REVEILLON[1] AND LUC VERVISCH[2]

[1]University of Rouen, CORIA-LMFN UMR-CNRS 6614, Avenue de l'Université, 76801 Saint Etienne du Rouvray, France
reveillon@coria.fr

[2]INSA of Rouen, CORIA-LMFN UMR-CNRS 6614, Avenue de l'Université, 76801 Saint Etienne du Rouvray, France
vervisch@coria.fr

(Received 5 July 2004 and in revised form 11 February 2005)

Spray combustion is analysed using a full simulation of the continuous gaseous carrier phase, while dilute-spray modelling is adopted for the discrete phase. The direct numerical simulation of the flow is performed in an Eulerian context and a Lagrangian description is used for the spray. The numerous physical parameters controlling spray flames are first studied to construct two synthetic model problems of spray combustion: a laminar spray flame that propagates freely over a train of droplets and a weakly turbulent spray-jet with coflowing preheated air. It is observed that the flame structures can be classified with respect to three dimensionless quantities, which characterize the fuel/air equivalence ratio within the core of the spray-jet, the ratio between the mean distance between the droplets and the flame thickness, and the ratio between an evaporation time and a flame time. A large variety of reaction zone topologies is found when varying those parameters, and they are scrutinized by distinguishing between premixed and diffusion combustion regimes. Partially premixed combustion is observed in most of the spray-jet flames and the spray parameters that make the flame transition from non-premixed to premixed combustion are determined. A combustion diagram for dilute-spray combustion is then proposed from the identification of those various regimes.

## 1. Introduction

Many industrial devices involve turbulent combustion of an evaporating liquid phase. Progress in the design of such systems strongly relies on the accurate control of a long list of combinations of processes, starting from the injection of liquid fuel in the chamber that is rapidly followed by combustion. Even when the liquid fuel is fully atomized by the injector (no liquid sheets remaining), strongly coupled nonlinear phenomena determine the behaviour in the combustion chamber. Usually the flow is turbulent, leading to strong interactions between a wide range of velocity fluctuations and droplet sizes. The vapour fuel distribution is then influenced by macro-scale dispersion of the liquid phase, which is complemented by micro-scale molecular diffusion allowing for the reactants to meet in thin reaction zones. Three major questions emerge: How are the droplets dispersed and evaporated? How is fuel and oxidizer turbulent mixing organized in the presence of local vapour sources? And how do these two phenomena impact on the flame structure? It appears difficult to embrace the whole underlaying problems at once. To focus on some of them, it is

intended in this paper to carry out direct numerical simulations (DNS) of the gaseous phase of a well-defined synthetic reacting spray-jet problem. On varying the control parameters of the simplified configuration, various flame structures are observed and in the light of the DNS results, a spray combustion diagram is proposed to delineate combustion regimes. It is found that knowledge of those regimes may be useful to relate the major properties of spray flames to the main atomizers features.

Over the past few decades, DNS has been widely used in a large range of applications. First introduced for inert flow simulations (Rogallo 1981; Lee, Lele & Moin 1991) it has been extended to reactive flows to study non-premixed, partially premixed and premixed turbulent combustion of purely gaseous fluids (Givi 1989; Poinsot, Candel & Trouvé 1996; Vervisch & Poinsot (1998); Poinsot & Veynante (2001); Pantano, Sarkar & Williams 2003). DNS of dispersion of solid particles in homogeneous (Elgobashi & Truesdell 1992) and non-homogeneous (Ling *et al.* 1998) turbulence has also been performed. The DNS/particles formulation was then extended to study the effects of evaporating droplets on the mixture fraction topology (Mashayek 1998; Miller & Bellan (1999, 2000); Réveillon & Vervisch 2000). However, very few works have been dedicated to DNS of two-phase flow combustion (Mashayek 1999, 2000).

Direct numerical simulation is based on the complete solution of all length and time scales generated by the fluid mechanics balance equations. Though the resolution techniques of a purely gaseous flow are now well established, the presence of an evaporating liquid phase cannot be treated simultaneously without modelling the subgrid effects associated with this discrete phase. The ratio of density and the dynamics of the liquid interface make a complete gas and liquid simulation very difficult, although it has been shown to be possible with very few droplets (Calimez 1998). A large variety of methods have been proposed to account for a dispersed phase in numerical simulations, see for instance the reviews by Faeth (1983) and Shirolkar, Coimbra & McQuay (1996). In the simulations discussed below, a full DNS of the carrier phase is achieved, but the flow inside and around the drops cannot be resolved. The droplets are local sources of fuel, whose properties are calculated in a Lagrangian context, whereas the compressible Navier–Stokes equations are solved in the Eulerian context. In addition to the basic limitations of DNS, the accurate treatment of the two-way coupling between the two phases imposes new restrictions, and the range of applicability of our simulations is limited to dilute sprays.

Two pioneering works have envisioned classifications of spray flame morphology. The first diagram (figure 1), developed by Chiu and coworkers (Suzuki & Chiu 1971; Chiu & Liu 1977; Chiu & Croke 1981; Chiu, Kim & Croke 1982) consisted in the determination of the structure of flames propagating through a cloud of droplets plunged in a preheated oxidizer. Spray combustion regimes were classified according to a group combustion number $G$. This dimensionless number may be seen as the ratio between the characteristic evaporation speed and the molecular diffusion speed, or the convective speed of the hot gases inside the cloud. When the Péclet number is large, Candel *et al.* (1999) showed that, in most cases, the relation $G \approx 5N^{2/3}/S$ between the group number $G$, the total number of droplets in the cloud $N$ and the separation parameter $S$ is satisfied. This last number, $S = \delta_s/\delta_{r_f}$, is the ratio between $\delta_s$, the mean droplet spacing, and $\delta_{r_f}$, a characteristic diffusion flame radius (Kerstein & Law 1982). In the case of high dilution (the volume of the liquid phase much smaller than the volume of the gaseous phase), the droplet mean spacing, $\delta_s = d^{-1/3}$, is directly determined from the droplet density $d$, that is the number of droplets per unit of volume. The length $\delta_{r_f}$ denotes the radius of a diffusion flame surrounding a single

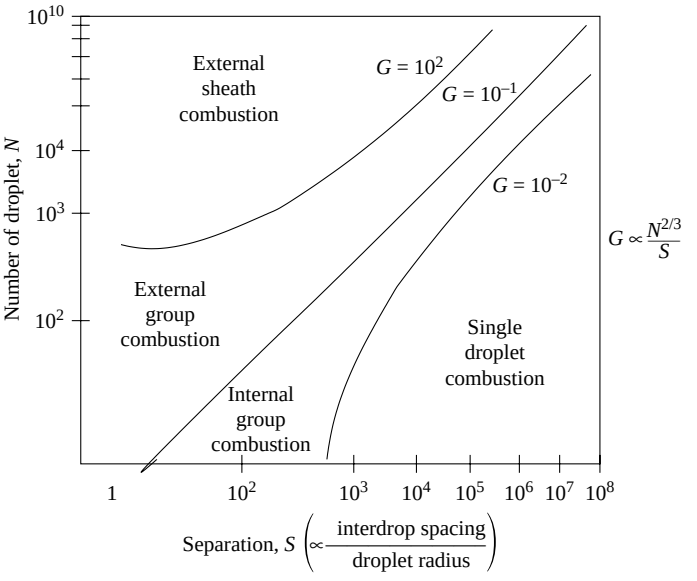


FIGURE 1. Group combustion diagram (Chigier 1983; Kuo 1986).

vaporizing drop in a quiescent oxidizer and having the mean properties of the spray (radius and evaporation time). When the separation number $S$ decreases, there is a point where the flame topology evolves from individual droplet combustion to group combustion. For a given value of $S$, on varying $N$, the number of drops in the liquid cloud, two major modes (figure 2) of spray combustion may be identified with respect to the group number $G$. In the first case, $G \gg 1$, the droplets are too close to each other to allow diffusion of heat inside the cloud. Only an external layer of droplets is evaporated and the resulting flame remains at a standoff distance from the spray boundary. Under the other limit condition, $G \ll 1$, the droplets are sparse enough so that the hot gases reach the core of the spray. Hence, evaporation and combustion processes take place around every individual droplets. Those conditions delineate the so-called 'external' combustion regime expected for $G \gg 1$, which is complemented by the 'internal' combustion regime, observed for $G \ll 1$ (figure 2). A smooth transition between these limit regimes was anticipated by Chiu *et al.* (1982), leading to intermediate submodes depending on the magnitude of $G$. When $G$ is slightly above unity, the flame stays around the droplet group with a temperature rise of the liquid phase affecting the core of the cloud. For $G$ smaller than unity, a first ring of individual burning droplets is centred on a droplet cloud surrounded by a diffusion flame.

Later, Chang and also Borghi and coworkers (Chang 1996; Borghi 1996*a*,*b*; Borghi & Champion 2000) added to the analysis the control parameters of the reaction zone itself, namely the characteristic flame time $\tau_f$ and its thickness $\delta_f$. In addition, the mean evaporation delay $\tau_v$ was introduced. When $\tau_v \ll \tau_f$, the mixture may locally be premixed and a propagating premixed flame develops (figure 3*a*). This regime should be observed for all values of mean droplet spacing $\delta_s$ and flame thickness $\delta_f$. In practice, the equivalence ratio of the mixture may not be fully uniform and a weakly varying partially premixed front propagates. If the evaporation time is large enough, for $\delta_f > \delta_s$, the collection of drops penetrates the reacting diffusive layers since the flame is broader than the mean droplet spacing $\delta_s$. This situation should

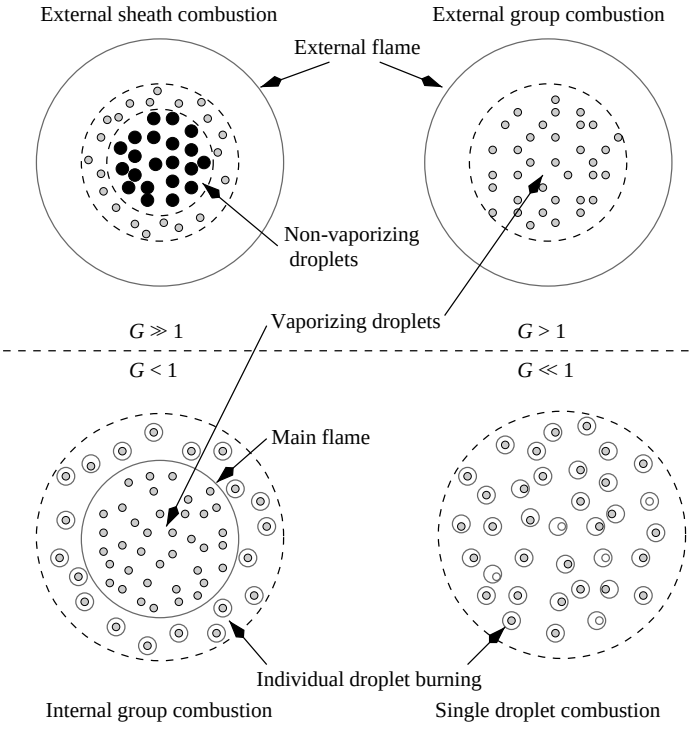


FIGURE 2. Combustion modes of a droplet cloud (Chiu *et al.* 1982; Kuo 1986).

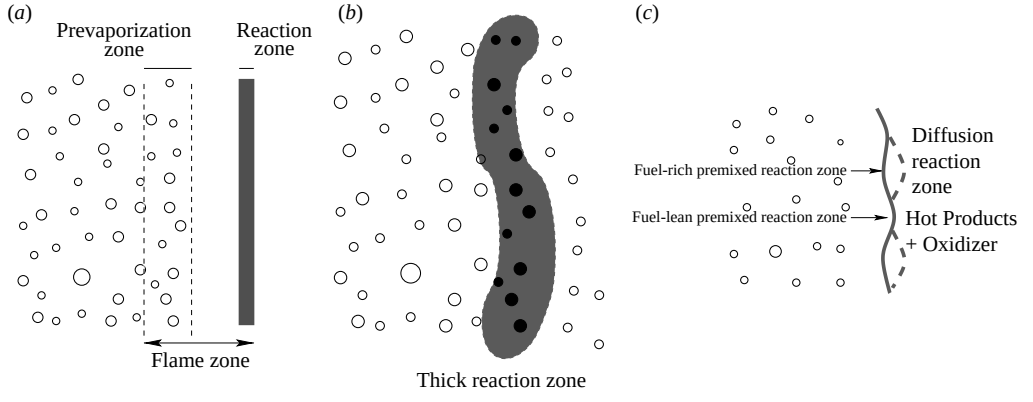


FIGURE 3. Laminar flame structures, limit cases (Borghi 1996*a*). (*a*) Prevaporized spray flame. (*b*) Thick flame. (*c*) Back flame zone.

rapidly promote the thickening of the flame (figure 3*b*). Aside from these extreme cases, the separation number ($S$) should be introduced. After the propagation of a primary partially premixed front, some droplets may remain, leading to a secondary (or back-flame) reaction zone (figure 3*c*). The topology of this secondary combustion zone depends on the magnitude of $S$. For small values of $S = \delta_s/\delta_{r_f}$, the droplets are burning individually or are clustered in small groups surrounded by a flame. This is called the 'group' combustion regime. As a complement, Borghi has distinguished

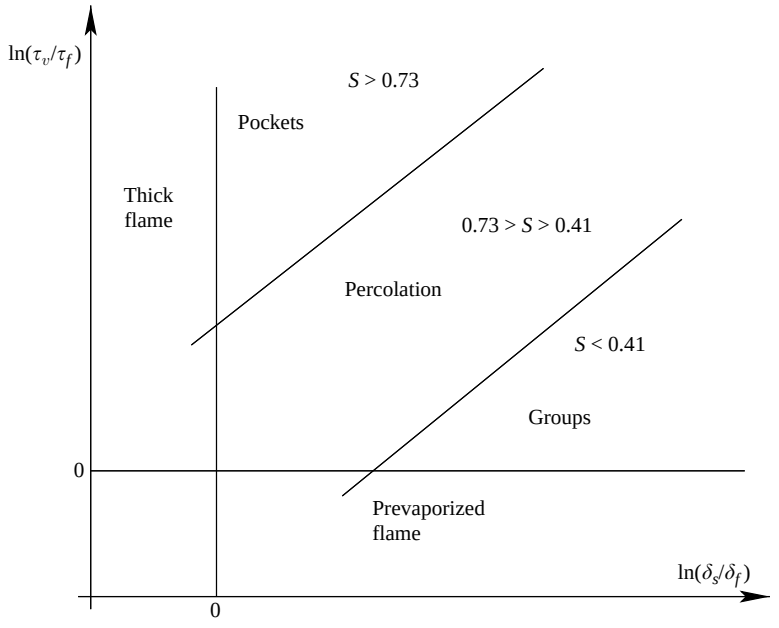


FIGURE 4. Borghi's diagram for laminar flames propagating in homogeneous and polydispersed droplets (Borghi 1996*a*).

a 'percolation' combustion regime and a 'pocket' combustion regime subsequently appearing when the separation number $S$ increases (figure 4).

Chiu and coworkers and Borghi and coworkers have defined these flame structures in the case of a quiescent spray without considering the global liquid fuel/air mass ratio. However, within a real spray combustion system, this key ratio is known to modify flame stability along with the overall properties of the combustion chamber. Changing it would affect the distribution of the local equivalence ratio of the gaseous mixture. Specifically, the topology of the primary and secondary reaction zones may vary significantly with this additional parameter. For instance, local extinctions may be observed due to local equivalence ratios outside the flammability limits. Moreover, the droplets and the mixture composition are also sensitive to advection, which plays a crucial role in spray combustion. Flame pictures can thus hardly be anticipated fully from those quiescent flow analyses, but they constitute a first basis on which additional effects can be included.

To make progress in spray flame characterization, the DNS reported below have been organized so that the equivalence ratio, the evaporation delay and the droplet mean spacing are varied for a well-defined, but simplified, spray-jet problem burning in a coflowing stream of air. In the subsequent sections, the flow configuration and the control parameters are given together with a careful description of the governing equations and of the numerous hypotheses that need to be formulated. Specific attention is paid to the artificial numerical coupling between the dispersed phase and the continuous carrier phase. Two configurations are studied: a freely propagating partially premixed laminar spray flame and a spray-jet flame evolving in a heated air coflow. Various flame structures are then reported from the DNS database and an attempt is made to organize them in a spray combustion diagram.

## 2. Model problems

A jet with a preheated and pulsed coflow of air was selected as the main computational configuration of this work. However, before performing complex simulations involving spray, weak turbulence and combustion, preliminary computations were carried out to investigate laminar spray flame propagation mechanisms and related flame topologies. To define the key parameters of simulations, the geometry of the weakly turbulent spray-jet is first detailed. The laminar configuration involving a freely propagating spray flame is then described.

### 2.1. *Weakly turbulent spray-jet flame*

The DNS focus on the behaviour of flames located downstream of a liquid injector, where the liquid sheet has been fully atomized and where the reaction zones are fed by an evaporating droplet-jet. In many combustion devices, stabilization results from the injection of swirling oxidizer in a confined geometry. Flames are stabilized by intense mixing generated by vortices recirculating hot gases trapped within the system. To mimic, in the DNS, some of the effects induced by the energy transported by recirculation zones, the diluted spray evolves within a preheated coflow of air. To hasten jet destabilization, the oxidizer inlet velocity profile is artificially forced with a frequency close to the natural unstable mode of the jet. This procedure allows control of the birth of the large scales at the edge of the spray and thus the initial mixing of the evaporating droplets. For clarity, coflow pulsations are fixed for all cases of the DNS database; only the properties of the liquid phase have been varied. Two-dimensional simulations are carried out although the evaporation process is kept three-dimensional. This would correspond to a thin slice of a three-dimensional planar jet with regularly spaced droplets in the third direction. A two-dimensional configuration is a limitation that is imposed by the large amount of information that is needed for capturing the spray evolution with high-order resolution of the carrier phase. Because it is intended to vary the control parameters of the simulations to seek various flame structures, three-dimensional simulations were not possible for all cases. Moreover, costless (i.e. small computational time) temporal (periodic) simulations were avoided since they do not allow study of flame stabilization. To limit the impact of the two-dimensional character of the simulations, the mean convective Mach of the planar shear flow under study is kept small and simulations are restricted to the field very close to injection.

#### 2.1.1. *Jet properties*

Many interactions between droplets, vortices and flames occurred during the simulations. To intelligibly analyse and compare the physical phenomena involved, the number of varying parameters has been minimized. The central spray-jet has a maximum velocity $U_J$ of the order of $20\,\mathrm{m\,s^{-1}}$, while the two coflowing oxidizer jets are forced with two sinusoidal signals having a phase lag of $\pi$. The averaged velocity of the air jets is $U_J$ and the amplitude of their fluctuations is $U_J/3$. The forcing period, $\tau_J = S_t\delta_J/2U_J$, is determined from $S_t = 0.4$, the Strouhal number of the central jet, and $\delta_J$ denotes the central jet width, which is of the order of 1 mm (figure 5). The properties of the injected spray (injected droplet-jet equivalence ratio $\Phi^I_{L0}$, droplet density $d^I$ and mean evaporation delay $\tau_v$) are varied to generate a DNS database of spray-jet combustion.

The DNS solver operates in non-dimensionalized units. When normalized with $\delta_{J/2}$, the jet half-width, or with $\delta_f$, the stoichimetric laminar and planar gaseous pre-mixed flame thickness, the computational domain length and height are:

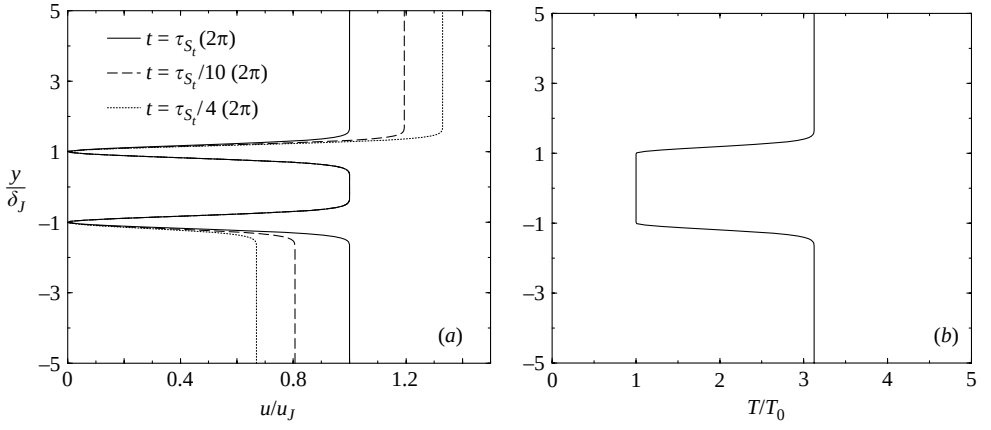


FIGURE 5. Inlet ($x = 0$) profiles. (*a*) Time-dependent velocity. (*b*) Temperature distribution.

$L_x = 14.22\delta_{J/2} = 102.6\delta_f$ and $L_y = L_x/2$, respectively. They are discretized on a Cartesian grid ($N_x = 513$ and $N_y = 257$).

The flame Zeldovitch Reynolds number $Re_f = \delta_f S_L/\nu$ is of the order of 4. With a characteristic stoichiometric flame speed for n-heptane $S_L \approx 0.4\,\mathrm{m\,s^{-1}}$, the flame thickness is then of the order of $\delta_f = Re_f \nu/S_L = 1.4 \times 10^{-4}$ m. The characteristic mesh size is $h = \delta_f/10$ and $L_x \approx 7$ mm and $L_y \approx 3.5$ mm. Similarly, the droplets have a radius of the order of 7 μm, and are thus smaller than the mesh size $h = L_x/N_x = 13.6$ μm. All quantities are made non-dimensional using a flame time $\tau_f = \nu/S_L^2$ and the characteristic flame length $\delta_f$.

2.1.2. *Spray properties*

Droplets are injected within the central jet. Their properties are in equilibrium with the surrounding carrier phase (similar velocity and temperature). They are initially monodispersed, but the combined evaporation and mixing effects rapidly lead to a polydispersed spray inside the computational domain. When the droplet surface reaches 1/1000 of its injection value, its contribution becomes negligible. Then, the droplet is removed from the computation, while the remaining small mass of liquid fuel is repartitioned as vapour on the surrounding Eulerian nodes.

The stoichiometric mass ratio of the reaction $s_r = (m_O/m_F)_s$ is used to define two equivalence ratios of the mixture. One concerns the liquid fuel/oxidizer mass ratio measured in the injected spray-jet, the other deals with the ratio of total mass of reactants injected in the overall computational domain. The introduction of two equivalence ratios for the same combustion problem is motivated by the use of diluted spray. When entering the computational domain, the diluted droplet-jet already contains a given amount of entrained air, which controls the equivalence ratio of the injected spray. This spray-jet is then mixed with the additional air surrounding the injected droplets. The total mass flow rate of liquid fuel is denoted $\dot{m}_F$. The equivalence ratio of the injected liquid spray-jet $\Phi^I_{L0}$ and of the whole injection $\Phi^B_{L0}$ may be defined as follows:

$$\Phi^I_{L0} = s_r \frac{\dot{m}_F}{\dot{m}^I_O} \quad \text{and} \quad \Phi^B_{L0} = s_r \frac{\dot{m}_F}{\dot{m}^I_O + \dot{m}^C_O}, \tag{2.1}$$

where $\dot{m}^I_O$ and $\dot{m}^C_O$ are the oxidizer mass flow rates of the central spray-jet and of the oxidizer coflow respectively. Because the overall oxidizer mass flow rate is fixed

| Name | $s_0/\delta_f^2$ | $\tau_v/\tau_f$ | $St=\tau_p/\tau_J$ | $\Phi_{L0}^I$ | $d^I$ |
|---|---|---|---|---|---|
| EXT-1 | $2.37\times10^{-4}$ | $2.6\times10^{-2}$ | $4.37\times10^{-2}$ | 0.87 | 248 |
| EXT-2 | $2.59\times10^{-4}$ | $2.84\times10^{-2}$ | $4.8\times10^{-2}$ | 1.00 | 248 |
| GROUP-1 | $2.81\times10^{-4}$ | $3.1\times10^{-2}$ | $5.2\times10^{-2}$ | 1.13 | 248 |
| HYBRID-1 | $3.37\times10^{-4}$ | $3.7\times10^{-2}$ | $6.2\times10^{-2}$ | 1.48 | 248 |
| HYBRID-2 | $3.91\times10^{-4}$ | $4.3\times10^{-2}$ | $7.2\times10^{-2}$ | 1.85 | 248 |
| EXT-3 | $4.96\times10^{-4}$ | $5.4\times10^{-2}$ | $9.2\times10^{-2}$ | 2.65 | 248 |
| EXT-4 | $1.77\times10^{-3}$ | 0.19 | 0.33 | 0.87 | 41 |
| EXT-5 | $1.94\times10^{-3}$ | 0.21 | 0.36 | 1 | 41 |
| GROUP-2 | $2.10\times10^{-4}$ | 0.23 | 0.39 | 1.13 | 41 |
| DIFF-1 | $2.52\times10^{-3}$ | 0.28 | 0.47 | 1.48 | 41 |
| HYBRID-3 | $2.93\times10^{-3}$ | 0.32 | 0.54 | 1.85 | 41 |
| EXT-6 | $3.7\times10^{-3}$ | 0.41 | 0.69 | 2.65 | 41 |
| EXT-7 | $3.5\times10^{-3}$ | 0.38 | 0.65 | 0.87 | 25 |
| EXT-8 | $3.83\times10^{-2}$ | 0.42 | 0.71 | 1.00 | 25 |
| GROUP-3 | $4.16\times10^{-3}$ | 0.46 | 0.77 | 1.13 | 25 |
| GROUP-4 | $5\times10^{-3}$ | 0.55 | 0.92 | 1.48 | 25 |
| DIFF-2 | $5.78\times10^{-3}$ | 0.64 | 1.07 | 1.85 | 25 |
| PREM-1 | $7.34\times10^{-3}$ | 0.81 | 1.35 | 2.65 | 25 |

TABLE 1. Summary of the weakly turbulent spray-jet simulations: $s_o$, surface of droplets at injection; $\delta_f$, stoichiometric premixed flame thickness; $\tau_v$, evaporation time; $\tau_f$, stoichiometric premixed flame time; $\tau_p$, kinetic time of the droplet at injection; $\tau_J$, forcing period of the jet; $St$, droplet Stokes number at injection; $\Phi_{L0}^I$, equivalence ratio in the spray-jet at injection; $d^I$, dilution factor at injection expressed in flame units.

for all the simulations, $\Phi_{L0}^I$ and $\Phi_{L0}^B$ are linearly linked through $\Phi_{L0}^I/\Phi_{L0}^B=(\dot{m}_O^I+\dot{m}_O^C)/\dot{m}_O^I=9.65$.

The spray-jet equivalence ratio, $\Phi_{L0}^I$, is one of the three major varying parameters of the simulations. It allows study of several regimes of spray flames, from the lean extinction limit up to very rich combustion. However, for a prescribed value of $\Phi_{L0}^I$, the injected liquid phase may be composed of many small droplets or a few big drops. To refine the description of the initially monodispersed spray, an additional density parameter $d^I$ has been introduced to quantify the number of droplets per unit of volume in the spray-jet. The volume of the injected drop is given by

$$v_d=\frac{1}{d^I}\frac{\dot{m}_F/\rho_d}{\dot{m}_F/\rho_d+\dot{m}_O^I/\rho} \tag{2.2}$$

where $\rho$ denotes the gaseous density and $\rho_d$ the liquid density. Because diluted sprays are studied $\dot{m}_O^I\gg\dot{m}_F$ and one may write

$$v_d\approx\frac{1}{d^I}\frac{\rho}{\rho_d}\frac{\dot{m}_F}{\dot{m}_O^I}=\frac{1}{d^I}\frac{\rho}{\rho_d}\frac{\Phi_{LO}^I}{s_r}. \tag{2.3}$$

The surface $s_0$ of the injected droplets may then be directly deduced from

$$s_0=(6\sqrt{\pi}v_d)^{2/3}\approx\left(6\sqrt{\pi}\frac{1}{d^I}\frac{\rho}{\rho_d}\frac{\Phi_{LO}^I}{s_r}\right)^{2/3}. \tag{2.4}$$

The evaporation delay $\tau_v$ is linearly related to $s_0$, as discussed below.

Simulations have been carried out with three droplet densities, $d^I=25, 41, 248$, given in flame units (number of droplets/$\delta_f^3$) and six spray-jet equivalence ratios, $\Phi_{L0}^I=0.87, 1, 1.13, 1.48, 1.85, 2.65$, leading to 18 configurations summarized in table 1.

| Name | $s_0/\delta_f^2$ | $\tau_v/\tau_f \ll 1$ | $\Phi_{L0}^I$ | $d^I$ |
|---|---|---|---|---|
| LAM-1 | $7.0 \times 10^{-5}$ | $3.1 \times 10^{-2}$ | 1.13 | 248 |
| LAM-2 | $8.43 \times 10^{-5}$ | $3.7 \times 10^{-2}$ | 1.48 | 248 |
| LAM-3 | $9.78 \times 10^{-5}$ | $4.3 \times 10^{-2}$ | 1.85 | 248 |
| LAM-4 | $1.24 \times 10^{-4}$ | $5.4 \times 10^{-2}$ | 2.65 | 248 |

TABLE 2. Summary of the laminar simulations (see table 1 for parameter description).

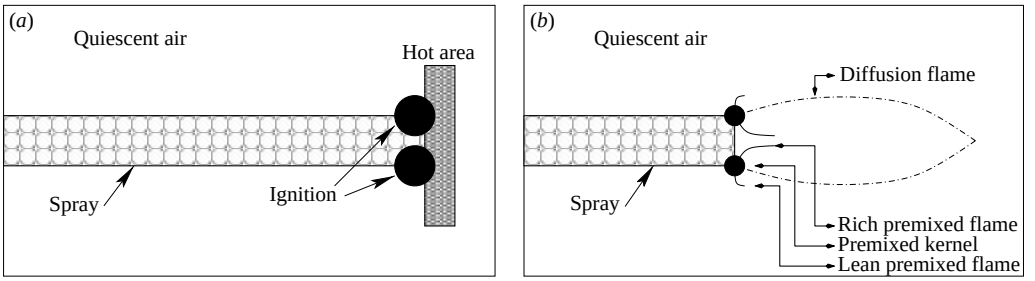


FIGURE 6. Sketch of the laminar simulation. (*a*) Ignition by energy deposit. (*b*) Flame propagation (fuel rich case).

The three droplet densities may be related to three group numbers ($G \approx 1, 2, 60$, respectively) corresponding to external combustion modes as defined by Chiu and coworkers (Suzuki & Chiu 1971; Chiu & Liu 1977; Chiu & Croke 1981; Chiu *et al.* 1982).

### 2.2. *Freely propagating laminar spray flame*

Four reference laminar cases (table 2) are also considered to seek the basic structures of flames propagating within a spray-jet. The spray properties are similar to those discussed above in terms of equivalence ratio, evaporation delay and droplet density. The domain size and grid are also kept the same; however, the gaseous flow is now quiescent (null initial velocity), with a uniform temperature (fresh gases temperature $T_0$). A train of width $\delta_J$ of droplets was inserted in the centre of the computational domain (figure 6) and a flame was ignited after a local temperature rise in the far end of the domain. Analyses are carried out far from the ignition area, when the flame reaches a stationary state with a constant upstream propagation velocity.

## 3. Transport, evaporation and combustion of spray

As mentioned in the introduction, a Lagrangian approach is adopted to follow the spray evolution within the gaseous oxidizer, which is described within an Eulerian context with the Navier–Stokes set of equations. Additional source terms have been introduced to allow for a two-way coupling between both liquid and gas phases.

### 3.1. *Dispersed phase: governing equations*

Because of the high density ratio between liquid and gas phases ($\rho_d/\rho = 684$), only drag forces have been considered to describe droplet dynamics. Moreover, several of the usual assumptions have been formulated. First, the spray is dispersed and each droplet is unaware of the existence of the others either with respect to its motion or evaporation. Any internal liquid circulation or droplet rotations are neglected and an

infinite heat conduction coefficient is assumed. Therefore, the liquid core temperature remains uniform in every droplet considered although it may vary as a function of time. The spray is then composed of local sources of mass following the saturation law and modifying momentum and gaseous fuel topology, depending on the local temperature, pressure and vapour mass fraction.

3.1.1. *Position and velocity*

Denoting the velocity and position vectors of every droplet $k$ by $\boldsymbol{V}_k$ and $\boldsymbol{X}_k$, respectively, the relations

$$\frac{\mathrm{d}\boldsymbol{V}_k}{\mathrm{d}t} = \frac{1}{\beta_k^{(V)}}(\boldsymbol{U}(\boldsymbol{X}_k, t) - \boldsymbol{V}_k), \tag{3.1}$$

$$\frac{\mathrm{d}\boldsymbol{X}_k}{\mathrm{d}t} = \boldsymbol{V}_k, \tag{3.2}$$

are used to track their evolution throughout the computational domain. The vector $\boldsymbol{U}$ represents the gas velocity at the droplet position $\boldsymbol{X}_k$. The right-hand-side term of equation (3.1) stands for a drag force applied to the droplet and $\beta_k^{(V)}$ is a kinetic relaxation time:

$$\beta_k^{(V)} = \frac{\rho_d a_k^2}{18 Cu_k \mu^*} \tag{3.3}$$

where $a_k$ is the diameter of the droplet $k$. A corrective coefficient $Cu_k = 1 + Re_k^{2/3}/6$ (Crowe, Sommerfeld & Tsuji 1998) is introduced to allow for the variation of the drag factor according to the value of the droplet Reynolds number $Re_k = \rho|\boldsymbol{U}(\boldsymbol{X}_k, t) - \boldsymbol{V}_k|a_k/\mu$.

3.1.2. *Heating and evaporation*

The heating and evaporation of every droplet in the flow may be described through a normalized quantity $B_k$, called the 'mass transfer number'. $B_k$ is the normalized flux of gaseous fuel between the droplet surface, where the fuel mass fraction takes the value $Y_k^s$, and the surrounding gas at the droplet position, where the fuel mass fraction is $Y_F(\boldsymbol{X}_k)$. It may be written

$$B_k = \frac{Y_k^s - Y_F(\boldsymbol{X}_k)}{1 - Y_k^s}. \tag{3.4}$$

By solving the mass and energy balance equations at the surface of a vaporizing droplet in a quiescent atmosphere (Kuo 1986), the following relations for the surface and the temperature evolution of droplet $k$ are found:

$$\frac{\mathrm{d}a_k^2}{\mathrm{d}t} = -\frac{a_k^2}{\beta_k^{(a)}}, \tag{3.5}$$

$$\frac{\mathrm{d}T_k}{\mathrm{d}t} = \frac{1}{\beta_k^{(T)}}\left(T(\boldsymbol{X}_d) - T_k - \frac{B_k L_v}{C_p}\right). \tag{3.6}$$

Again, characteristic relaxation times appear. They are defined by

$$\beta_k^{(a)} = \frac{S_c}{4Sh_c}\frac{\rho_d}{\mu^*}\frac{a_k^2}{\ln(1 + B_k)}, \tag{3.7}$$

$$\beta_k^{(T)} = \frac{P_r}{6Nu_c}\frac{C_d}{C_p}\frac{\rho_d a_k^2}{\mu^*}\frac{B_k}{\ln(1 + B_k)}. \tag{3.8}$$

Normalized gas and liquid heat capacities are denoted $C_p$ and $C_d$ respectively and, like $L_v$, the latent heat of evaporation, they are constant in the simulations ($C_p/C_{p0}=1$, $C_d/C_p=4$ and $L_v/(C_{p0}T_0)=2.67$ where $C_{p0}$ is the air heat capacity and $T_0=300\,\mathrm{K}$ the fresh gases temperature). The Schmidt $Sc$ and Prandtl $Pr$ numbers are both equal to 0.7. $Sh_c$ and $Nu_c$ are the convective Sherwood and Nusselt numbers, respectively. They are both equal to 2 in a quiescent atmosphere, but a correction has to be applied in a convective environment. In this context, the empirical expression of Faeth and Fendell (Kuo 1986), identical either for $Sh_c$ or $Nu_c$ ($Sh_c \,|\, Nu_c$), has been used:

$$(Sh_c \,|\, Nu_c)_k = 2 + \frac{0.55 Re_k (S_c \,|\, P_r)_k}{\left(1.232 + Re_k (S_c \,|\, P_r)_k^{4/3}\right)^{1/2}}. \tag{3.9}$$

One of the most accurate models to describe the evaporation process is to consider a phase equilibrium at the interface thanks to the saturation law of Clausius–Clapeyron:

$$\frac{\mathrm{d}\ln\left(P_k^s\right)}{\mathrm{d}T} = \frac{L_v}{r_F T^2}, \tag{3.10}$$

where $r_F$ is the perfect gas constant in the gaseous fuel, leading to the following expression for the partial pressure $P_k^s$ of fuel vapour at the surface of every droplet:

$$P_k^s = P_{ref} \exp\left(-\frac{L_v}{r_F}\left(\frac{1}{T_k^s} - \frac{1}{T_{ref}}\right)\right), \tag{3.11}$$

where $P_{ref}$ and $T_{ref}$ are two reference parameters. The n-heptane boiling temperature $T_{ref}=371.6\,\mathrm{K}$ corresponding to a unity reference pressure $P_{ref}=1$ atm has been used. $T^s$ is the gas temperature at the droplet surface. The liquid temperature is uniform in all droplets. Thus, it is equal to the temperature of the gas at the interface $T_k^s = T_k$.

The gaseous fuel mass fraction at the surface of the droplet may be determined using

$$Y_k^s = \left(1 + \frac{W_O}{W_F}\left(\frac{P(\boldsymbol{X}_d)}{P_k^s} - 1\right)\right)^{-1}, \tag{3.12}$$

where $W_O$ and $W_F$ are the molecular weights of the oxidizer and fuel considered respectively ($W_F/W_O=3.46$). Once the gaseous fuel mixture fraction at the droplet surface is known, the varying number $B_k$ is determined by introducing relation (3.12) into equation (3.4). Consequently, equations (3.5) and (3.6), describing the evolution of droplet surface and temperature, are closed.

### 3.2. *Continuous phase: governing equations*

The choice has been made to use fully compressible direct numerical simulations of the gas phase evolution. The turbulence stays small, but all the spectra of turbulent structures that are present are accurately resolved. The carrier phase is air treated as a compressible Newtonian fluid following the equation of state for a perfect gas. The instantaneous balance equations describe the evolution of mass $\rho$, momentum $\rho\boldsymbol{U}$, total energy $E_t$ and species mass fraction. $Y_F$ denotes the mass fraction of gaseous fuel resulting from spray evaporation and $Y_O$ is the oxidizer mass fraction. The following set of balance equations are solved where usual notation is adopted:

$$\frac{\partial \rho}{\partial t} + \frac{\partial \rho U_k}{\partial x_k} = \dot{m}, \tag{3.13}$$

$$\frac{\partial \rho U_i}{\partial t} + \frac{\partial \rho U_i U_k}{\partial x_k} = -\frac{\partial P}{\partial x_i} + \frac{\partial \sigma_{ik}}{\partial x_k} + \dot{v}_i, \tag{3.14}$$

$$\frac{\partial \rho E_t}{\partial t} + \frac{\partial (\rho E_t + P) U_k}{\partial x_k} = \frac{\partial}{\partial x_k}\left(\lambda \frac{\partial T}{\partial x_k}\right) + \frac{\partial \sigma_{ik} U_k}{\partial x_i} + \rho \dot{\omega}_e + \dot{e}, \tag{3.15}$$

$$\frac{\partial \rho Y_F}{\partial t} + \frac{\partial \rho Y_F U_k}{\partial x_k} = \frac{\partial}{\partial x_k}\left(\rho D \frac{\partial Y_F}{\partial x_k}\right) + \rho \dot{\omega}_F + \dot{m}, \tag{3.16}$$

$$\frac{\partial \rho Y_O}{\partial t} + \frac{\partial \rho Y_O U_k}{\partial x_k} = \frac{\partial}{\partial x_k}\left(\rho D \frac{\partial Y_O}{\partial x_k}\right) + \rho \dot{\omega}_O, \tag{3.17}$$

with

$$\sigma_{ij} = \mu\left(\frac{\partial U_i}{\partial x_j} + \frac{\partial U_j}{\partial x_i}\right) - \frac{2}{3}\mu \frac{\partial U_k}{\partial x_k}\delta_{ij},$$

together with the equation of state for perfect gases:

$$P = \rho r T.$$

Source terms are present, the $\dot{\omega}_i$ terms are related to the chemical reaction processes and $\dot{m}$, $\dot{\boldsymbol{v}}$, $\dot{e}$ result from a two-way coupling between the carrier phase and the spray.

3.2.1. *Spray and chemical source terms*

The terms $\dot{m}$, $\dot{\boldsymbol{v}}$, $\dot{e}$ modify the gas phase, mass, momentum and temperature owing to a distribution of the Lagrangian quantities on the Eulerian grid. Every droplet has positive or negative source terms to be distributed over the Eulerian nodes and the organization of an accurate projection of those Lagrangian sources onto the Eulerian mesh is not an easy task. In real spray flow, this distribution is not instantaneous and further assumptions are needed to perform the simulations. Every Lagrangian source is distributed over the Eulerian nodes by adding the volumic contributions from droplets. This induces a numerical dispersion that remains weak because of the small size of the DNS grid (Réveillon & Vervisch 2000). It would be possible to introduce a diffusion delay before repartitioning the evaporation sources over the Eulerian nodes. However, it cannot be the ultimate solution since it is possible that droplets cross a flame front and, with this additional diffusion delay, an artificial fuel ballast could be created with a non-burning gaseous fuel stored in a combustion zone, which is not fully satisfactory either and could have an impact on flame structure.

For every Eulerian node, a control volume $\mathscr{V}$ is defined by the mid-distance to the neighbour nodes. Because an isotropic Cartesian grid of mesh size $h$ has been used, the volume $\mathscr{V}$ is defined by $\mathscr{V} = h^3$. Even in the two-dimensional simulations, this cubic definition is kept to ensure that they may be viewed as slices of planar three-dimensional configurations, with evaporating three-dimensional droplets. The mass source term $\dot{m}$ applied to the Eulerian node $n$ is denoted $\dot{m}^{(n)}$:

$$\dot{m}^{(n)} = \frac{1}{\mathscr{V}} \sum_k \alpha_k^{(n)} \frac{\mathrm{d}m_k}{\mathrm{d}t} \tag{3.18}$$

where $\sum_k$ is the sum over every droplet inside the volume $\mathscr{V}$ and affecting the Eulerian node $n$ considered. $\alpha_k^{(n)}$ is the repartition coefficient of the $k$ droplet source term on the node $n$. Considering all the nodes affected by the droplet $k$, it is necessary to have $\sum_n \alpha_k^{(n)} = 1$ to conserve mass, momentum and energy during the Lagrangian/Eulerian coupling. Values of $\alpha_k^{(n)}$ are chosen as the regressive normalized distance between the droplet and every surrounding node. They correspond to the coefficients that would be used to interpolate linearly any value of the Eulerian nodes at the droplet position. $m_k$ is the mass of the $k$ droplet considered in the neighbourhood of the node. It is

defined by $m_k = \rho_d \pi a_k^3/6$ and, using equations (3.5) and (3.18), one may write

$$\dot{m}^{(n)} = \rho_d \frac{\pi}{4} \frac{1}{\mathscr{V}} \sum_k \alpha_k^{(n)} a_k^3 / \beta_k^{(a)}. \tag{3.19}$$

Similarly, the relation

$$\dot{\boldsymbol{v}}^{(n)} = \frac{1}{\mathscr{V}} \sum_k -\alpha_k^{(n)} \frac{\mathrm{d} m_k \boldsymbol{V}_k}{\mathrm{d}t}, \tag{3.20}$$

leads to the expression of the momentum source term:

$$\dot{\boldsymbol{v}}^{(n)} = -\rho_d \frac{\pi}{4} \frac{1}{\mathscr{V}} \sum_k \alpha_k^{(n)} a_k^3 \left( \frac{2}{3} \frac{\boldsymbol{U}(\boldsymbol{X}_d, t) - \boldsymbol{V}_k}{\beta_k^{(V)}} - \frac{\boldsymbol{V}_k}{\beta_k^{(a)}} \right). \tag{3.21}$$

The energy variation of the gaseous flow induced by the droplets inside the volume $\mathscr{V}$ may be written

$$\dot{e}^{(n)} = \frac{1}{\mathscr{V}} \sum_k -\alpha_k^{(n)} \frac{\mathrm{d} m_k C_d T_k}{\mathrm{d}t}, \tag{3.22}$$

and it may be developed as

$$\dot{e}^{(n)} = -C_d \rho_d \frac{\pi}{4} \frac{1}{\mathscr{V}} \sum_k \alpha_k^{(n)} a_k^3 \left( \frac{2}{3} \frac{T(\boldsymbol{X}_d, t) - T_k - B_k L_v / C_p}{\beta_a^{(T)}} + \frac{T_k}{\beta_k^{(a)}} \right). \tag{3.23}$$

An oversimplified description of the chemistry is used. All species considered are assumed to have identical properties, diffusion coefficients and heat capacities. An Arrhenius law is obtained from an automated method that generates a single-step kinetics which reproduces exactly the response of the flame speed versus equivalence ratio (Vervisch, Labegorre & Réveillon 2004). This is done by making the pre-exponential parameter $K(\phi)$ a direct function of the local equivalence ratio $\phi$. The energy, fuel and oxidizer chemical source terms ($\dot{\omega}_e$, $\dot{\omega}_f$ and $\dot{\omega}_o$, respectively) are then obtained from

$$\dot{\omega} = \rho K(\phi) Y_F Y_O^{11} \exp(-T_a/T) \tag{3.24}$$

giving the rate of a single-step kinetics of n-heptane oxydation:

$$\mathrm{C_7H_{16}} + 11\mathrm{O_2} \rightarrow 7\mathrm{CO_2} + 8\mathrm{H_2O}. \tag{3.25}$$

$T_a$ is the activation temperature. When a planar unstrained premixed flame at equivalence ratio $\phi$ is computed with equation (3.24) it propagates at the n-heptane burning velocity $S_L(\phi)$ as given by Linán & Williams (1993). A heat release coefficient $\alpha$ is defined by $\alpha = (T_b - T_0)/T_b = 0.8$ where $T_b$ is the adiabatic flame temperature for a non-preheated mixture and $T_0$ is the fresh gases temperature.

Accordingly, the source terms in the set of Eulerian equations (3.13)–(3.17) may be written $\dot{\omega}_F = -W_F \dot{\omega}$, $\dot{\omega}_O = -11 W_O \dot{\omega}$, and $\dot{\omega}_e = \alpha (1 + \Phi_s) \nu_F \dot{\omega} / (\gamma - 1)(1 - \alpha)$ where $\Phi_s = (11 W_O / W_F)(Y_{F,o} / Y_{O,o}) = 15$ with $W_O = 32\,\mathrm{g\,mol^{-1}}$, $W_F = 100\,\mathrm{g\,mol^{-1}}$, $Y_{F,o} = 1$ and $Y_{O,o} = 0.23$, where the molar weights and the free-stream conditions are thus those of pure gaseous n-heptane burning in air. The usual definition of the mixture fraction $Z$ is chosen. A passive scalar is defined as $\varphi = s_r Y_F - Y_O$ (Linán & Williams 1993), where the stoichiometric mass ratio is $s_r = 11$ for the single-step reaction given by equation (3.25). Normalizing $\varphi$ yields the mixture fraction $Z = (\Phi_0 (Y_F / Y_{F,o}) - (Y_O / Y_{O,o}) + 1)/(\Phi_0 + 1)$. Notice that in the case of sprays, $Z$ cannot reach unity, but a local maximum level depending on the saturation conditions. The gaseous

equivalence ratio used to define the pre-exponential function may then be written $\phi(Z) = \Phi_s Z/(1-Z)$.

The sixth-order PADE scheme of Lele (1992) and the Navier–Stokes characteristics boundary conditions (NSCBC) of Poinsot & Lele (1992) were used to solve the gas-phase transport equations on the Cartesian mesh. The time integration of both spray and gas-phase equations is done with a third-order-explicit Runge–Kutta scheme with a minimal data storage method (Wray 1990). A third-order interpolation is employed when gaseous-phase properties are needed at the droplet positions.

## 4. Laminar spray flames

### 4.1. *Introduction*

The structure of laminar flames propagating around clusters of droplets in a quiescent atmosphere is first analysed. Because the simulations involve dilute spray, the carrying phase of the fuel droplets is composed of air and the equivalence ratio within the spray-jet varies from $\Phi^I_{L0} = 1.13$ to $\Phi^I_{L0} = 2.65$. As previously discussed, varying $\Phi^I_{L0}$ allows for study of the burning of a droplet-jet in which various amounts of air would have been entrained, after full atomization of the liquid. There is no mean convective velocity of the reactants in those simulations and freely propagating flames are observed whose structure depends solely on $\Phi^I_{L0}$, the composition of the quiescent surrounding air being fixed. The parameters of the laminar simulations are summarized in table 2. The characteristic evaporation delay, $\tau_v$, is related to the droplet surface:

$$\tau_v = \frac{S_c}{4Sh_c}\frac{1}{\ln(B_0+1)}\frac{\rho_d s_0}{\pi\mu} \quad \text{where} \quad B_0 = B(T = T_b, Y_F = 0, P = 1), \tag{4.1}$$

In these laminar simulations, $\tau_v$ remains small compared to $\tau_f$, the flame characteristic time. Thus, the fuel evaporates faster than it is consumed by the flame and the reaction zone propagates without any difficulty along the cloud of droplets. The combustion properties are steady in a frame moving with the flame front.

To analyse the burning mode, $\xi_p$, a normalized version of Takeno's flame index (Yakhot *et al.* 1986), is chosen:

$$\xi_p = \frac{1}{2}\left(1 + \frac{\nabla Y_F}{|\nabla Y_F|}\cdot\frac{\nabla Y_O}{|\nabla Y_O|}\right). \tag{4.2}$$

When $\xi_p$ vanishes, diffusion flames are observed, while premixed combustion is found when it reaches unity. More or less partially premixed reaction zones develop for values of $\xi_p$ ranging between zero and unity. To evaluate the amount of burning in premixed and partially premixed regimes and compare it to the overall heat release rate, a premixed fraction of the burning rate $W_p(x)$ may be introduced. $W_p(x)$ is defined for each streamwise location $x$, as the average, over the transverse flow direction $y$, of the amount of fuel burning in premixed modes normalized by the total burning rate:

$$W_p(x) = \frac{\int_y \xi_p \dot{\omega}\,\mathrm{d}y}{\int_y \dot{\omega}\,\mathrm{d}y}. \tag{4.3}$$

This quantity and other flame parameters are now used to seek combustion regimes observed in the laminar cases.

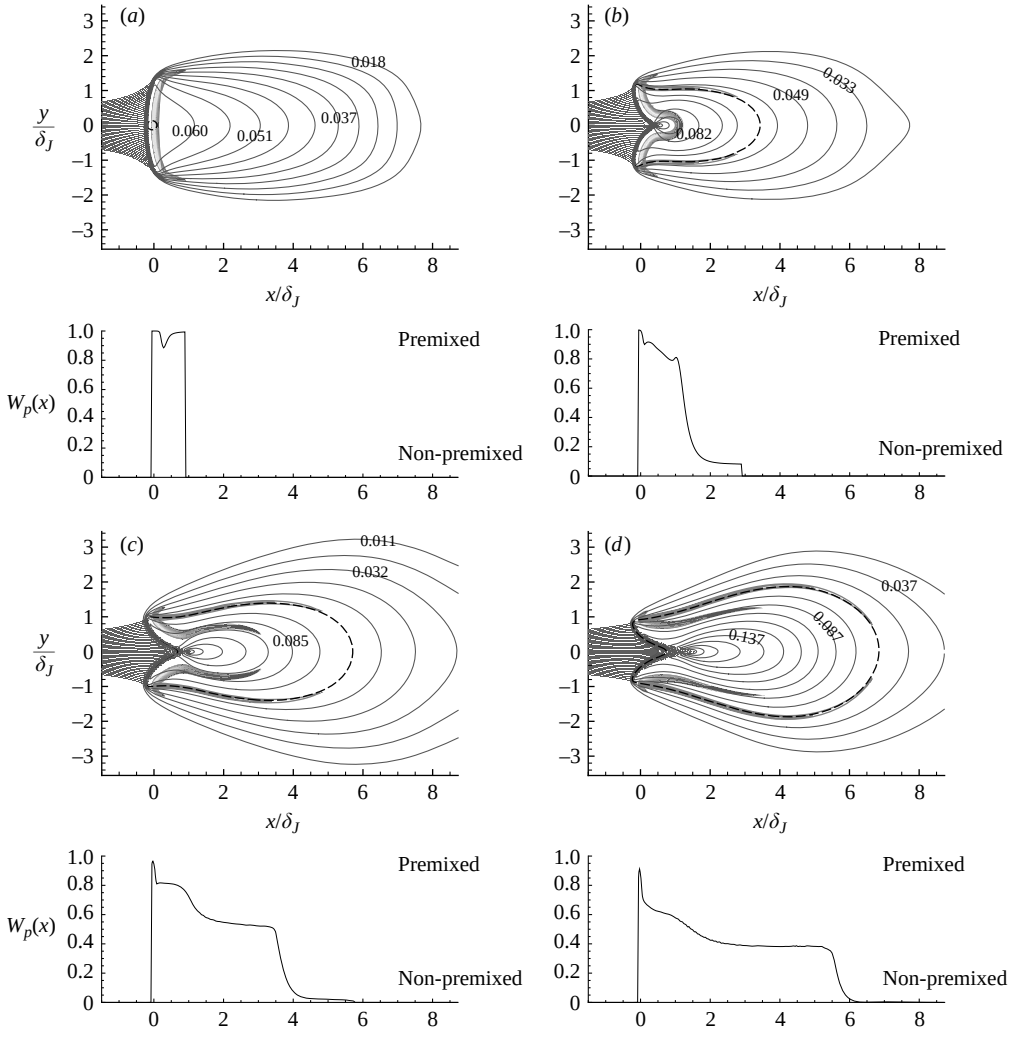


FIGURE 7. Laminar cases (table 2). Upper figures. Dots: droplets. Flooded grey area: premixed flame. Grey iso-contours: diffusion flame. Thin iso-contours: mixture fraction $Z$. Thick dashed line: stoichiometric mixture fraction $Z_s$. Lower figures: premixed fraction $W_p(x)$ (equation (4.3)). (*a*) LAM-1, (*b*) LAM-2, (*c*) LAM-3, (*d*) LAM-4.

### 4.2. *Laminar spray flame topology*

Figure 7 shows the flame structures observed in the four simulations. Not all the computational domain is presented in this figure and $x = 0$ has been chosen to be at the streamwise position of the maximum heat release. Even though the flow configuration is symmetrical, complete simulations of the whole domain have been carried out, demonstrating that the symmetry is numerically conserved. (A point that is a real issue in a fully compressible formulation of spray combustion.)

Partially premixed combustion is observed in the four cases (figure 7). Increasing the equivalence ratio of the spray-jet strongly modifies the flame structure. The flame evolves from a weakly varying partially premixed front up to a tribrachial (or triple-) flame, when the equivalence ratio is further increased. Figure 7(*a*) (case LAM-1 of table 2) shows that for $\Phi^B_{L0} = 1.13$, the mixture burns in a slightly lean premixed regime

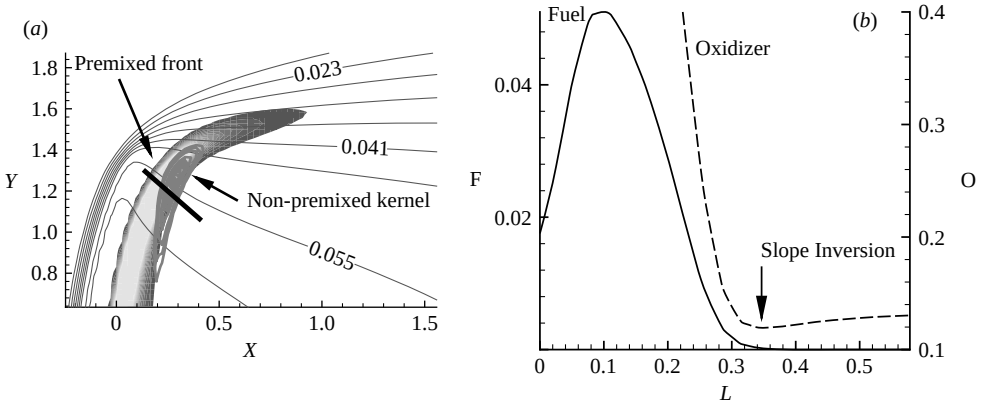


FIGURE 8. Detail of the edge-flame, premixed regime with an embryonal diffusion flame. (*a*) Reaction rate and mixture fraction iso-lines. (*b*) Fuel and oxidizer mass fraction distributions.

with a pre-evaporation front ahead of the flame. The premixed burning ratio $W_p$ (equation (4.3)) stays close to unity, except in a very localized kernel at the flame edges. Figure 8 shows a snapshot of one of the edge-flames along with the reactant profiles. When crossing the partially premixed front, both fuel and oxidizer have negative slopes. At the leading edge of the flame, the partially lean premixed flame is curved and the oxidizer can penetrate within the lean premixed flame. Then, the oxidizer slope becomes positive in a zone where some n-heptane is left, fuel and oxidizer come into contact and an embryonal diffusion flame develops. On increasing the equivalence ratio $\Phi^B_{L0}$, this embryo moves towards the stoichiometric line to evolve into the trailing diffusion flame found in case LAM-2, while the partially premixed front becomes highly curved. Hence, when the equivalence ratio is increased, the edges of figure 7(*a*) give birth to a trailing diffusion flame. This transition is observed in figure 7(*b*) when $\Phi^B_{L0} = 1.48$. The flame is decomposed into three parts: a stoichiometric triple point, and a very weak diffusion flame accompanied by a strongly burning rich premixed flame.

When the equivalence ratio reaches $\Phi^B_{L0} = 1.85$, the partially premixed flame is quenched at the centre of the spray-jet, to become the rich premixed branch (LAM-3 and LAM-4) of a fully developped triple-flame. In figure 7(*c*, *d*), $W_p$ illustrates the streamwise transition between the fully premixed propagating front and the trailing diffusion flame.

As discussed by Ruetsch, Vervisch & Liñán (1995) and Boulanger *et al.* (2003), the effect of heat release in gaseous partially premixed combustion is the deflection of the flow upstream of the curved front, which has a net result of making the triple-flame propagate faster than the stoichiometric burning velocity. This flow deflection promotes the appearance of weak vorticity ahead of the triple points. For the laminar cases, vorticity generated by the flame and mixture fraction field are presented in figure 9. Owing to the small mass of the droplets, their trajectories are deflected by the flame and the width of the spray is increased. It modifies the local equivalence ratio and affects the flame burning rate. The vorticity distribution is strongly modified when the diffusion flames develops. In cases LAM-2 and LAM-3, the droplet trajectories follow the streamlines, explaining the highly curved flame observed in figure 7(*b*). The accumulation of droplets along the axis of symmetry leads to locally high equivalence ratios when evaporation takes place, finally leading to the extinction of the too

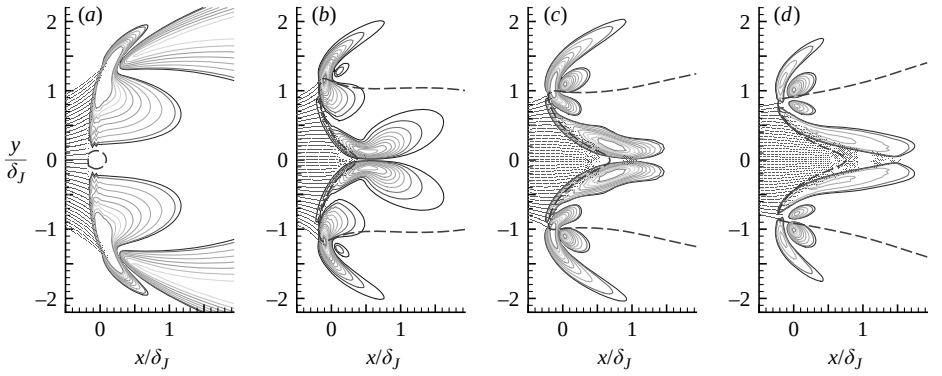


FIGURE 9. Vorticity induced by the spray-flame, laminar cases. Continuous lines: vorticity levels. Dotted lines: mixture fraction levels. Thick dashed line: iso-stoichiometric mixture fraction $Z_s$. (*a*) LAM-1, (*b*) LAM-2, (*c*) LAM-3, (*d*) LAM-4.

rich branch. This mechanism drives the evolution of flame structures observed in figure 7(*b*, *c*), where the two triple-flames become disconnected.

### 4.3. *Laminar spray flame structure in mixture-fraction space*

A complementary way to analyse the flame structure developing around the cluster of droplets consists of plotting (figure 10) the reactants $Y_F$ and $Y_O$ and the temperature versus the mixture fraction $Z$. The spray flame response versus $Z$ completely differs from the well-known gaseous diffusion flame. Figure 10(*d*, *e*, *f*) displays scatter plots of the flame response for the richest configuration (LAM-4). Figures 10(*a*, *b*, *c*) shows the lower limits of the scatter plots for all the laminar cases (LAM-1, 2, 3, 4). These figures may be understood by following the Lagrangian evolution of the spray mapped in mixture-fraction space. Each droplet starts to evaporate on penetrating the preheating zone of the flame. These droplets lead to gaseous fuel and oxidizer concentrations that travel along the frozen-flow mixing line of the mixture-fraction space, till ignition occurs. Within the flamability limits, many trajectories within the mixture fraction space start from the mixing line, well above the usual strained diffusion flame response (Peters 2000).

The slope of the scatter plot envelope and the maximum value of $Z$ reached depend on the initial equivalence ratio $\Phi_{L0}^I$ of the cluster of droplets and on the saturation properties of the liquid.

The heat release is plotted in figure 11 as a function of the mixture fraction. Non-premixed and premixed regimes are displayed. The diffusion flame is centred on the stoichiometric mixture fraction, with a global level of heat release of the order of 20 % of the heat release of the reference stoichiometric gaseous premixed flame. The premixed regime, however, reaches approximatively 90 % of this reference heat release rate. Moreover, even though the initial equivalence ratio of the cluster is rich ($\Phi_{L0}^I = 2.65$, LAM-4), the fast evaporation of the droplets promotes locations where the reactants are in stoichiometric proportions and, locally, fully burning stoichiometric flames always exist.

Four related main points emerge from this preparatory study based on laminar freely propagating spray flames. The amount of air within the core of the spray-jet modifies the equivalence ratio within the core of the jet and has a strong impact on the flame structure. Both partially premixed and diffusion flames are always observed. As expected, the transition between premixed and diffusion is found when the amount of

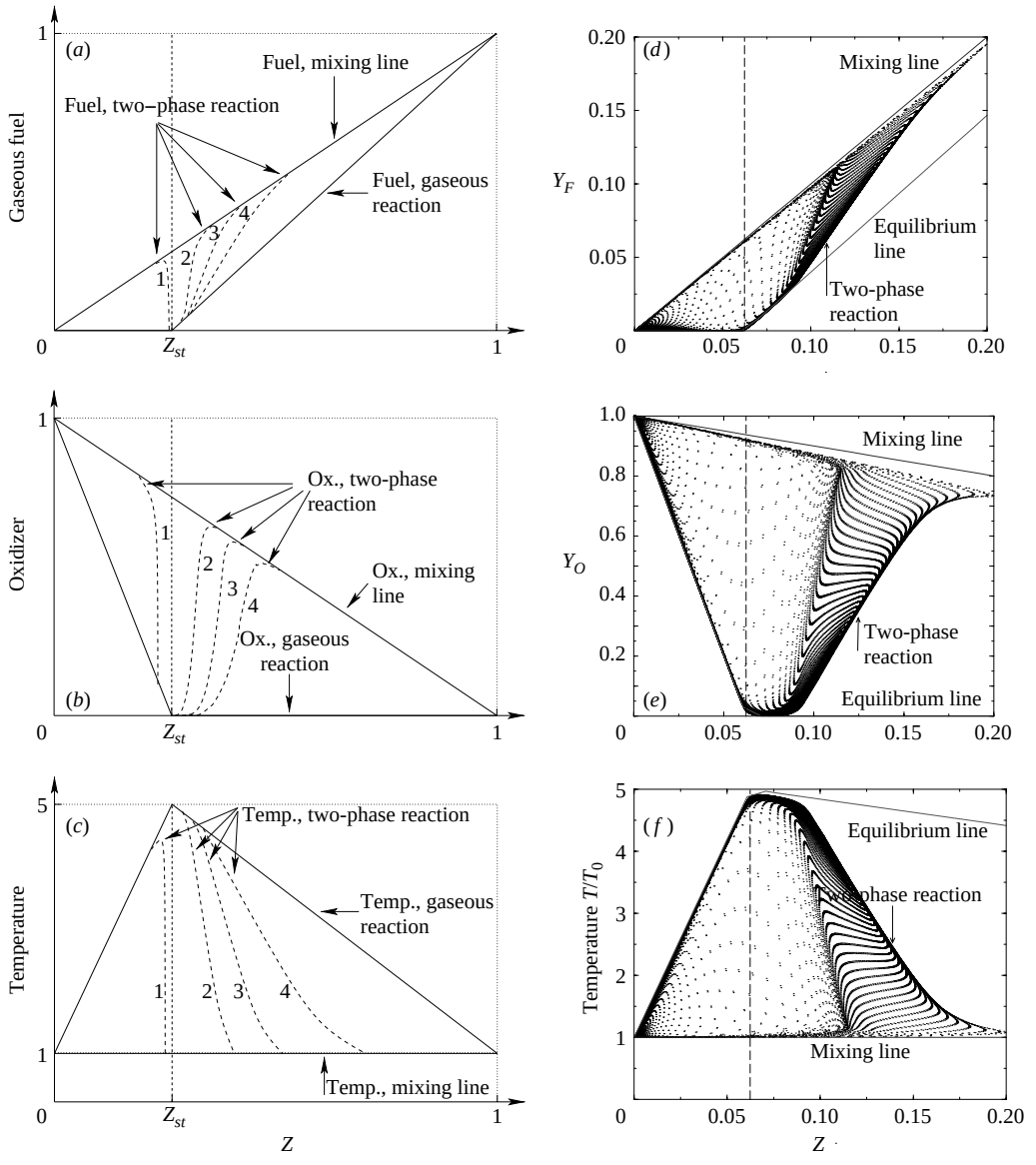


FIGURE 10. Flame structure in mixture-fraction space. (*a–c*) Lower limit of the scatter plots, Lines 1, 2, 3 and 4 correspond to LAM-1, LAM-2, LAM-3 and LAM-4 cases respectively (table 2). (*d–f*) Scatter plots in mixture-fraction space for LAM-4, (*d*) fuel mass fraction, (*e*) oxidizer, (*f*) temperature.

air within the droplet-jet decreases. When increasing the spray-jet equivalence ratio, the diffusion flame starts at the leading edge of the weakly varying partially premixed front to further evolve into a triple-flame-like structure.

## 5. Forced spray-jet flames

The analysis now focuses on combustion of spray-jets actuated by a forced heated air coflow ($T_c = 3T_0$). In the description of the laminar flame discussed above,

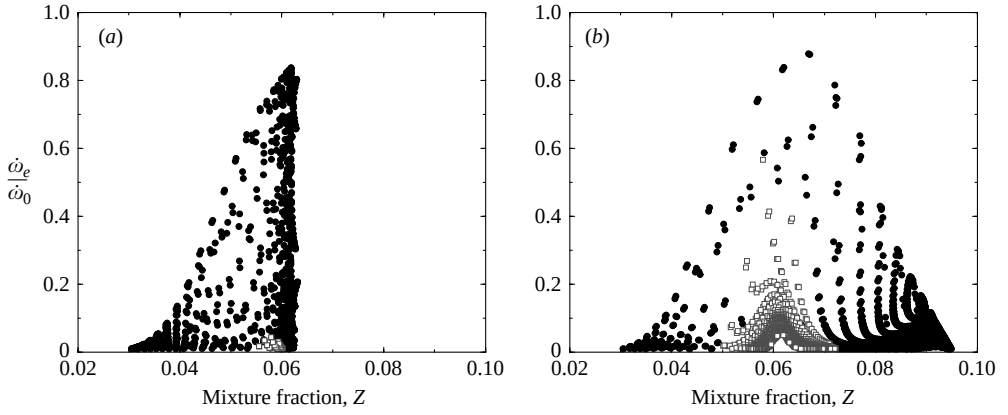


FIGURE 11. Heat release response in mixture fraction space, normalized by $\dot{\omega}_0$, a reference stoichiometric premixed flame burning rate. Solid circles: premixed regime. Hollow squares: diffusion regime. (*a*) LAM-1, (*b*) LAM-4.

combustion develops from a spray of droplets. Major flame structures are reported for this particular situation and are qualitatively compared with experimental observations, then combustion regimes are discussed.

Eigthteen cases are considered, the corresponding flame structures are classified following the two axes $(\Phi^I_{L0}, d^I)$ shown in figure 12. The vertical axis indicates the droplet-jet equivalence ratio $(\Phi^I_{L0})$ and the horizontal axis represents the density of the cluster of droplets $(d^I)$ and, incidentally, their evaporation delay (4.1) and (2.4). The characteristic times $\tau_t$ and $\tau_f$ are fixed in the simulations and the number of variables of the problem has thus been reduced by linearly relating $\tau_p$ and $\tau_v$, which are both functions of the droplet surface:

$$\frac{\tau_p}{\tau_v} = \frac{4}{9}\frac{\ln(1+B)}{Sc}. \tag{5.1}$$

In every cell of figure 12, flame snapshots showing premixed and diffusion regimes are presented along with the droplets for a given simulation time $t = 17.15\tau_f$. Two distinct flame evolutions are observed in figure 12. Along the vertical axis, starting from lean partially premixed combustion, the increase of the droplet-jet equivalence ratio $(\Phi^I_{L0})$ leads to the development of diffusion combustion. Along the horizontal axis, the decrease of $d^I$ (or $\tau_v/\tau_f$) promotes the appearance of numerous disconnected flame fronts.

### 5.1. *Weakly turbulent spray flame topology*

For the set of parameters that have been chosen, flame structures are first analysed for fixed values of $d^I$, the dilution (columns in figure 12). Lean flames are examined first ($\Phi^I_{L0} = 0.87$ and $\Phi^I_{L0} = 1$, table 1). The lean mixture is obtained by evaporating small droplets featuring a short evaporation delay. Close to the burning zone, the mixture fraction field never reaches its stoichimetric value in the three lean cases due to rapid mixing with air. Because of the preheating of the oxidizer coflow, weak autoignition in a lean diffusive regime occurs at the location of the most reactive mixture fraction isoline as previously reported from gaseous DNS by Mastorakos, Baritaud & Poinsot (1997). Those weakly burning diffusion flames appear ahead of the main partially premixed lean reaction zone.

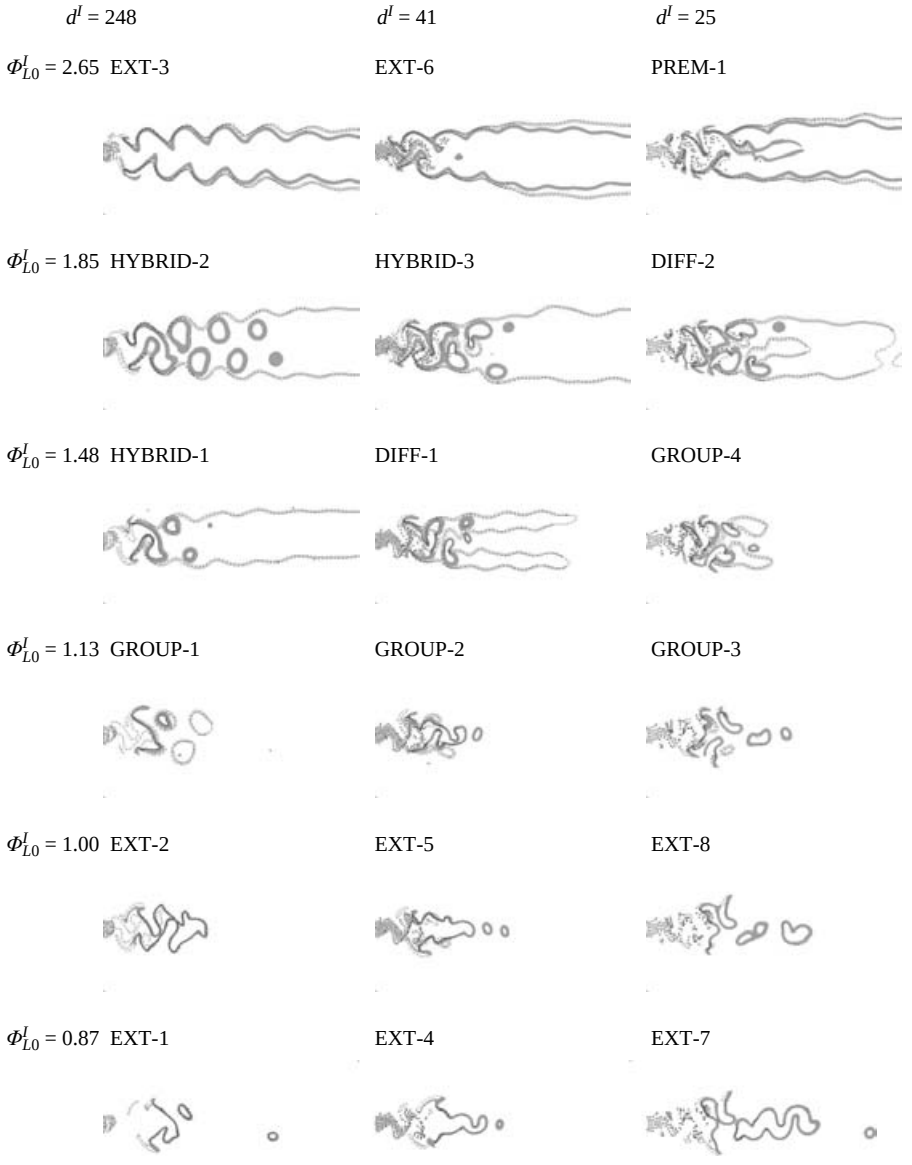


FIGURE 12. Summary of the weakly turbulent simulations. $\Phi^I_{L0}$: equivalence ratio in the spray-jet. $d^I$: spray dilution at injection expressed in flame units. Dark grey: premixed flames. Grey lines: diffusion flames. Symbols: droplets.

On slightly increasing the equivalence ratio ($\Phi^I_{L0} = 1$), by increasing the droplet size, a fuel-richer local mixture fraction may appear because coherent vortices can cause the heavier droplets to cluster. The local equivalence ratio may then increase up to the stoichiometric condition. Fast propagating premixed fronts ahead of trailing double-flames start to appear. The double-flame is composed of a diffusion flame burning the fuel left on the back of a rich premixed flame. Depending on the spray-jet local equivalence ratio, the separation distance between premixed and diffusion reaction zones is greater or smaller. To visualize the combustion modes easily, in addition

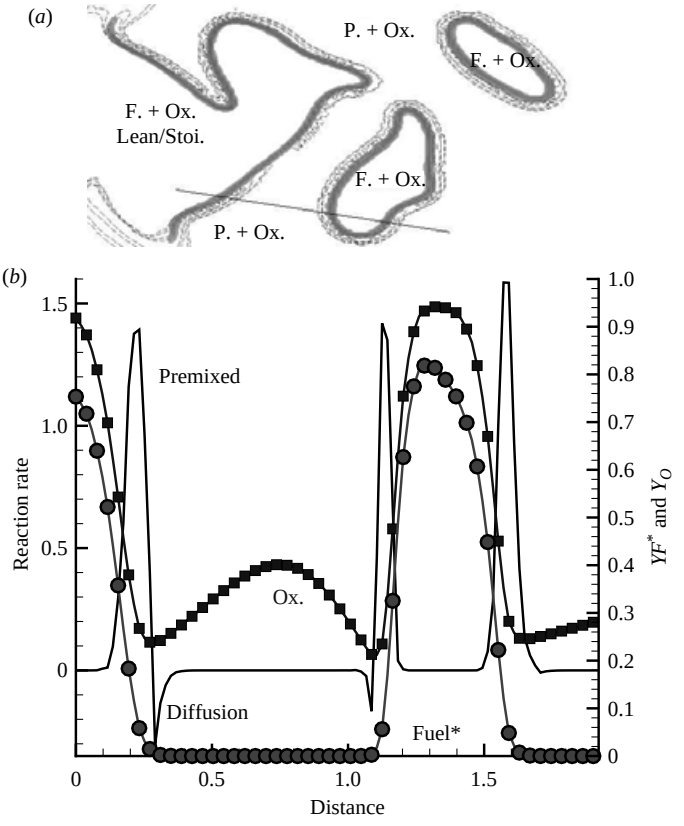


FIGURE 13. (*a*) Iso-contours of burning rate. Dark grey: premixed burning. Grey iso-contours: diffusion burning. (*b*) Profiles at location of the black line in (*a*). Circles: scaled fuel mass fraction $YF^* = Y_F \Phi_s$. Squares: oxidizer mass fraction. Line: flame index burning rate. Case EXT-1 (table 1).

to the flame index (equation (4.2)) and to the premixed fraction of the burning rate (equation (4.3)), in figure 13, $\dot{\omega}^*$, a flame index burning rate is introduced to clearly separate premixed and diffusion combustion in the analysis:

$$\dot{\omega}^* = \dot{\omega} \frac{\nabla Y_F \cdot \nabla Y_O}{|\nabla Y_F \cdot \nabla Y_O|}; \tag{5.2}$$

$\dot{\omega}^* = \dot{\omega}$ in the case of premixed combustion and $\dot{\omega}^* = -\dot{\omega}$ in diffusion flames, where $\dot{\omega}$ is the burning rate given by (3.24).

On further increasing the spray-jet equivalence ratio from $\Phi^I_{LO} = 1.13$ up to $\Phi^I_{LO} = 2.65$ (figure 12), non-premixed flames anchored to triple-points appear. The mixture fraction increases on the jet axis and a rich premixed flame develops. Local clusters of droplets have evaporated leading to pockets of fuel-rich mixture, which remain below the local saturation conditions. The combustion consumes the oxidizer in the pocket via a first rich premixed flame; then a stoichiometric diffusion flame is left around the remaining fuel blob. Accordingly, diffusion flame rings are convected downstream (figure 14(*a*): GROUP-1). For too large values of $\Phi^I_{LO}$, the burning velocity of the partially premixed rich mixture becomes too small to allow flame propagation and the rich reaction zone is pushed away from the centreline. The flame is then stabilized by a triple point and a stoichiometric diffusion flame develops on

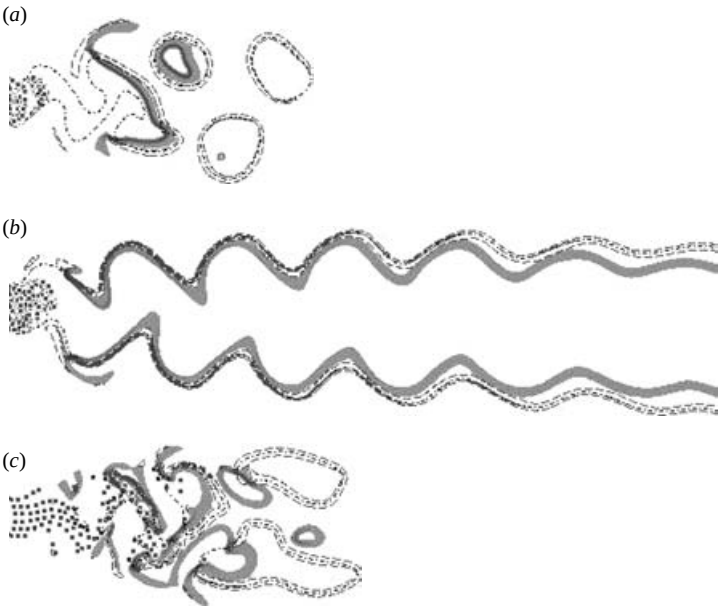


FIGURE 14. Details of weakly turbulent flame structures (table 1). Dots: droplets. Dark grey: premixed flame. Grey dashed iso-contours: diffusion flame. Thick dashed line: stoichiometric mixture fraction $Z_s$. (*a*) GROUP-1 ($\Phi^I_{L0} = 1.13$, $d^I = 248$). (*b*) EXT-3 ($\Phi^I_{L0} = 2.65$, $d^I = 248$). (*c*) GROUP-4 ($\Phi^I_{L0} = 1.48$, $d^I = 25$).

the back of the rich premixed front to consume the remaining fuel. A double-flame is then formed (figure 14(*b*): EXT-3). This global picture of the flame topology versus the spray-jet equivalence ratio holds for all spray dilution considered (figure 12).

Flame structures are now analysed when keeping the equivalence ratio constant and decreasing the spray dilution (rows in figure 12). The coexistence of both premixed and diffusion regimes, reported above, is not strongly affected by the change of $d^I$. However, their spatial distribution evolves with $d^I$. Diminishing the dilution leads to an increase of the characteristic evaporation delay $\tau_v$ and of the kinetic time $\tau_p$ (equation (5.1)). This promotes the appearance of clusters of droplets that are convected downstream to favour group burning (figure 14(*c*): GROUP-4). These clusters result from heavier droplets that have a large inertia and mainly follow the large-scale movement. Because of the resulting high clustering rate of the evaporating droplets, the mixture fraction may reach and locally exceed its stoichiometric level. Therefore, after the stabilizing front, the premixed flame fluctuates locally between lean and rich regimes and the diffusion flame is detached from the double-flame structure to form a ring-flame. Premixed and diffusion burning tend to be more clearly seperated as $d^I$ decreases.

In addition to this, a flame structure that is specific to dilute-spray combustion is also observed when the spray-jet equivalence ratio is large enough (DIFF-1: $\Phi^I_{L0} = 1.48$ and $d^I = 41$ in figure 12). The topology of the mixture field is then completely different from the one that would be observed in gaseous fuel-jet combustion. In the spanwise direction, three layers exist. In the centre of the jet, the oxidizer is mixed with fuel to a greater or lesser extent, depending on the spray-jet equivalence ratio. This first layer is surrounded by evaporated fuel that comes from droplets that have been flushed away from the central core of the spray-jet by the rolling up of the mixing

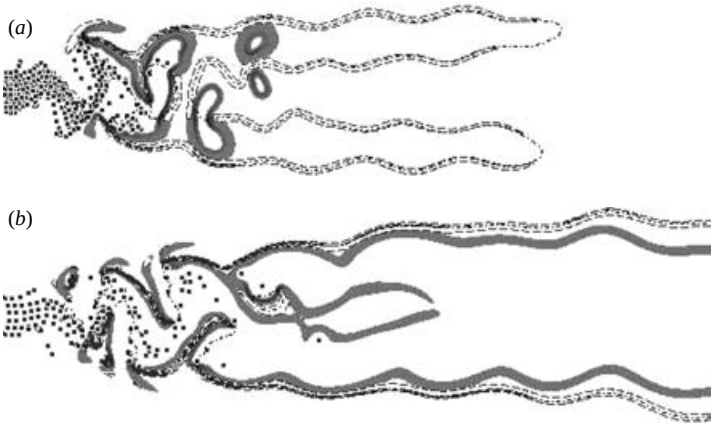


FIGURE 15. Weakly turbulent spray-jet flame, cases of table 1. Dots: droplets. Dark grey: premixed flame. Grey dashed iso-contours: diffusion flame. Thick dashed line: stoichiometric mixture fraction level $Z_s$. (*a*) DIFF-1 ($\Phi^I_{L0} = 1.48$, $d^I = 41$). (*b*) PREM-1 ($\Phi^I_{L0} = 2.65$, $d^I = 25$).

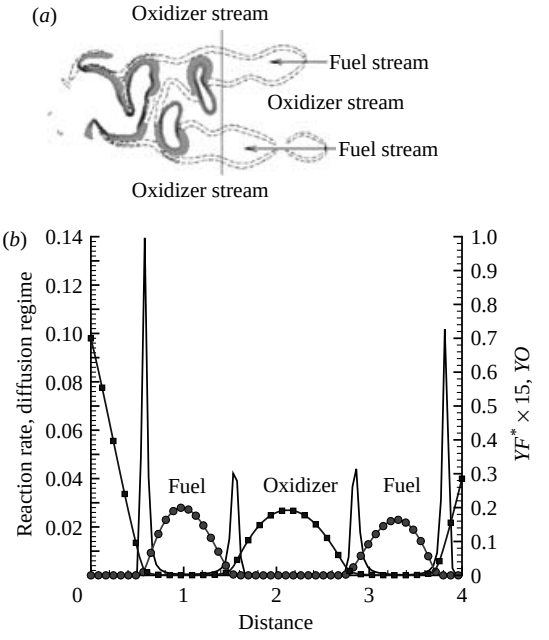


FIGURE 16. (*a*) Iso-contours of burning rate. Grey area: premixed burning. Dashed iso-contours: diffusion burning. (*b*) Profiles at location of the black line in (*a*). Circles: fuel mass fraction. Squares: oxidizer mass fraction. Line: flame index burning rate. Case DIFF-1 (table 1).

zone. These two layers are immersed within the coflowing oxidizer. In figure 15(*a*) (DIFF-1), two fuel layers have been generated by the rolling up of the shear layer and a central and an outer diffusion flame are formed. In figure 15(*b*) (PREM-1), where the equivalence ratio is much higher, two rich premixed flames exist, with a diffusion flame surrounding the outer premixed reaction zone. Those structure are detailed in figure 16 and 17 respectively.

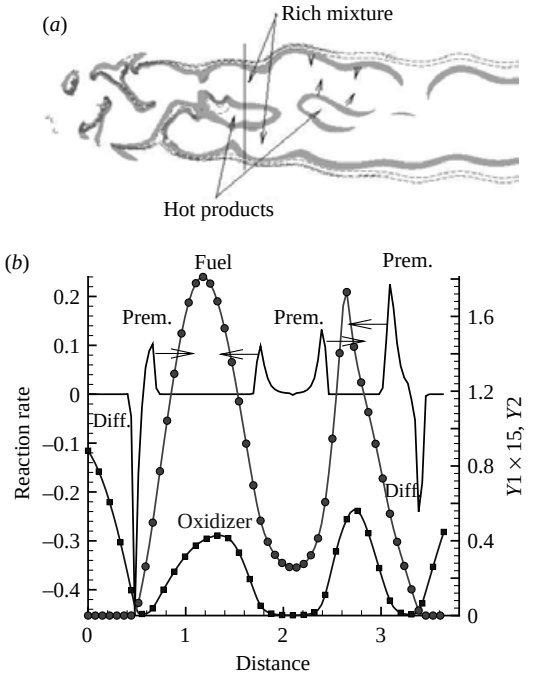


FIGURE 17. (*a*) Iso-contours of burning rate. Dark grey: premixed burning. Grey iso-contours: diffusion burning. (*b*) Vertical profiles at location of the hot products in (*a*). Circles: fuel mass fraction. Squares: oxidizer mass fraction. Line: flame index burning rate. Case PREM-1 (table 1).

Cessou & Stepowski (1996) have performed planar visualization of OH emissions in ethanol flames. It is always difficult to compare DNS with experiments, because of the former's numerous restrictions (Poinsot & Veynante 2001). However, the three major characteristic regimes found in the experiments are recovered in the DNS. They reflect the trends discussed above: spray jet equivalence ratios above unity lead to rich partially premixed combustion associated with diffusion flame burning and to an 'open external' combustion regime displayed in figure 18(*a*). Decreasing the spray-jet equivalence ratio within the flammability limits brings a 'hybrid' regime (figure 18*b*). The last case has motivated many discussions on spray-flame topologies, since it is not obvious how to determine the exact flame structure from the OH field which shows very intricate radical layers (figure 18*c*). The DNS of a burning mode featuring a central and an outer diffusion flame may be compared to this intriguing planar visualization, though it should be noticed that this comparison may be performed at a qualitative level only.

### 5.2. *Combustion diagram*

From DNS, the flame structures may be organized into three main categories, themselves possibly divisible into sub-groups.

(*a*) External combustion: this concerns combustion with a continuous flame interface. Two sub-regimes may be observed, depending on the location and topology of the reaction zone.

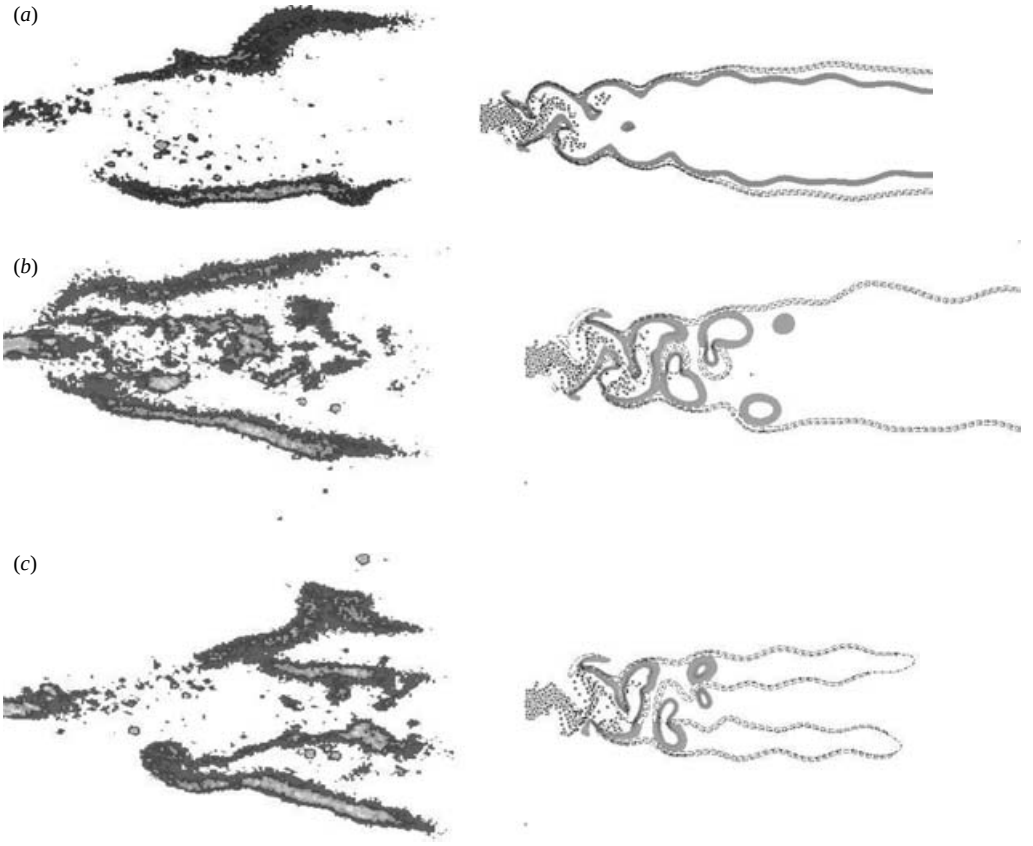


FIGURE 18. Qualitative analysis of spray-jet flames. Left: experiments by Cessou & Stepowski (1996). Right: DNS. (*a*) EXT-6 Open external regime, $\Phi^I_{Lo} = 2.65$ and $d^I = 41$. (*b*) HYBRID-3. Hybrid regime, $\Phi^I_{Lo} = 1.85$ and $d^I = 41$. (*c*) GROUP-2 Central diffusion flame, $\Phi^I_{Lo} = 1.48$ and $d^I = 41$ (table 1).

(i) A 'closed external' combustion regime, when a single flame front, mostly premixed, manages to engulf the droplets and their corresponding amount of evaporated gaseous fuel to transform it into products (figure 19*a*).

(ii) An 'open external' combustion regime, when two reaction zones develop on each side of the central jet (figure 19*b*).

(*b*) 'Group' combustion: the droplets are organized into several groups, with flames independently consuming each cluster. Both rich premixed and diffusion flames are observed (figure 19*c*).

(*c*) 'Hybrid' combustion: this regime is a combination of the two previous ones. The premixed flames are burning in a group combustion mode, whereas the diffusion flames cannot percolate between the clusters of droplets because of the too rich environment. The fuel left is burnt with the coflowing oxidizer in an additional external diffusion flame (figure 19*d*).

To illustrate these regimes, the premixed fraction of the burning rate $W_p(x)$ (equation (4.3)) is shown for the 'closed external' combustion regime in figure 20(*a*). This regime is generally associated with a lean premixed mixture. On the other hand, the heat released by the 'open external' type structure results from premixed and

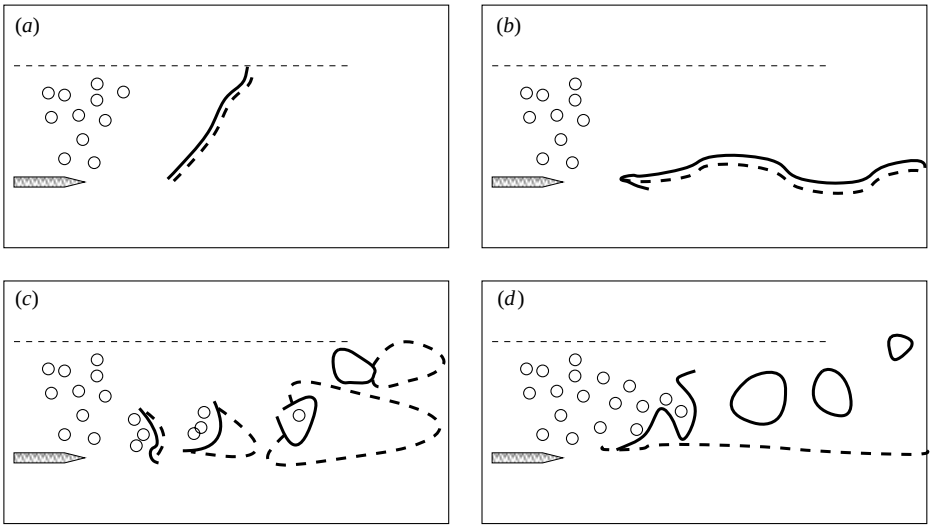


FIGURE 19. Summary of the generic flame structures. Continuous line: premixed burning. Dashed line: diffusion burning. (*a*) Closed external, (*b*) open external, (*c*) group, (*d*) hybrid.

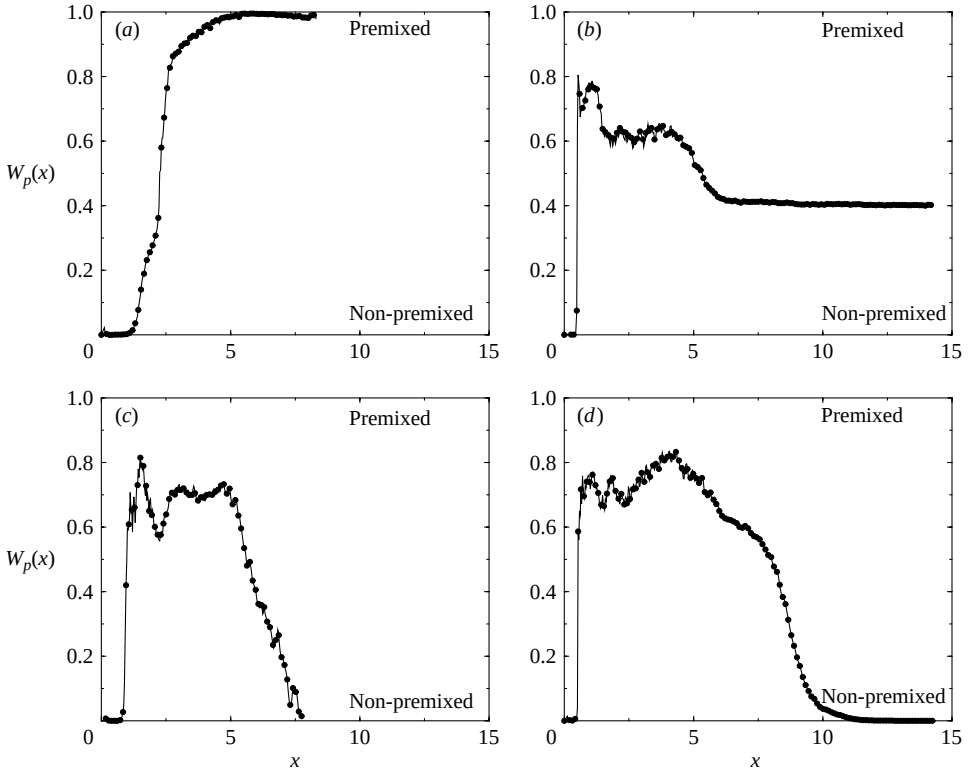


FIGURE 20. Premixed fraction of the burning rate $W_p(x)$ (equation (4.3)). (*a*) EXT-1. (*b*) EXT-6. (*c*) GROUP-4. (*d*) HYBRID-3 (table 1).

diffusion flames (figure 20*b*). The 'group' combustion case may be viewed as the more complex regime. After the usual premixed stabilizing leading edge-flames, premixed and diffusion pockets are formed. The last traces of fuel disappear within weakly burning diffusion flames (figure 20*c*). Eventually, the 'hybrid' regime is composed of a strongly burning premixed flame front that is followed by diffusion flame combustion (figure 20*d*).

These regimes may be organized on a combustion diagram, but at least three directions are necessary to classify them. The first concerns the ratio $\tau_v/\tau_f$ between characteristic evaporation and flame times. Another important ratio, $\delta_s/\delta_f$, is based on the mean distance between the droplets and the flame thickness, the droplet spacing $\delta_s$ being inversely related to $d^I$, the spray dilution. Finally, $\Phi^I_{L0}$ the equivalence ratio, measured within the spray-jet, is also needed to account for the amount of oxidizer entrained in the core of the central jet. It is important to note that the weak turbulence and the chemistry are fixed and similar for all cases, otherwise more parameters would be necessary.

To start the classification, the pioneering analysis by Borghi (1996*a*) is followed. If the evaporation delay of every injected droplet is very small compared to the flame characteristic time ($\tau_v/\tau_f \ll 1$) then purely gaseous combustion occurs. Therefore when $\tau_v/\tau_f \ll 1$, the droplets are vaporized far away from the flame front and combustion develops in a fully gaseous mode. The jet is thus a mixture of fuel vapour and oxidizer whose equivalence ratio depends on the initial droplet loading. A tentative combustion diagram for this partially premixed jet is presented in figure 21(*a*), where the six configurations with a short evaporation delay are shown. The main combustion modes discussed above are recovered by fixing $\delta_s$, the mean spacing of the droplets such as $d^I = 248$.

To discuss figure 21(*a*), the choice is made to travel in a direction where $\Phi_{L0}$ increases. This is done starting from the case $\Phi_{L0} = 0.87$ up to the simulation with $\Phi_{L0} = 2.65$, in figure 12. In the leanest case, a double flame is found. It is wrinkled but remains continuous around the fuel issuing from the spray evaporation, corresponding to a 'closed external' combustion regime, which is similar to a bunsen flame. As the injected equivalence ratio increases, local fluctuations of mixture fraction appear because of mixing of the fuel stream with the surrounding oxidizer. For a slightly rich injection $\Phi_{L0} = 1.13$, vapour-rich areas (or pockets) burn first in a premixed regime that consumes the carrying oxidizer, followed by diffusion flame rings organized between the remaining fuel and the external oxidizer. If the equivalence ratio increases to $\Phi_{L0} = 1.45$, there is still a premixed group combustion in the core of the jet to burn all the carrying oxidizer. However, enough fuel remains to maintain an external diffusion flame, leading to the 'hybrid' combustion regime. If the equivalence ratio increases again to $\Phi_{L0} = 2.65$, the central vapour/oxidizer mixture is too rich to allow the propagation of a premixed flame and both premixed and non-premixed fronts are pushed away from the core of the spray, to burn in the 'open external' combustion regime, which is very similar to a gaseous non-premixed jet flame.

When the evaporation delay increases ($\tau_v/\tau_f \leqslant 1$), droplets may reach the flame front but it is unlikely that they will cross the burning zone without being fully evaporated. However, because they may interact with the turbulent structures while releasing their vapour, the topology of the gaseous fuel may be highly non-uniform in most cases. The corresponding combustion diagram is proposed in figure 22(*b*). The positions of simulations are indicated on the graph for two different droplet

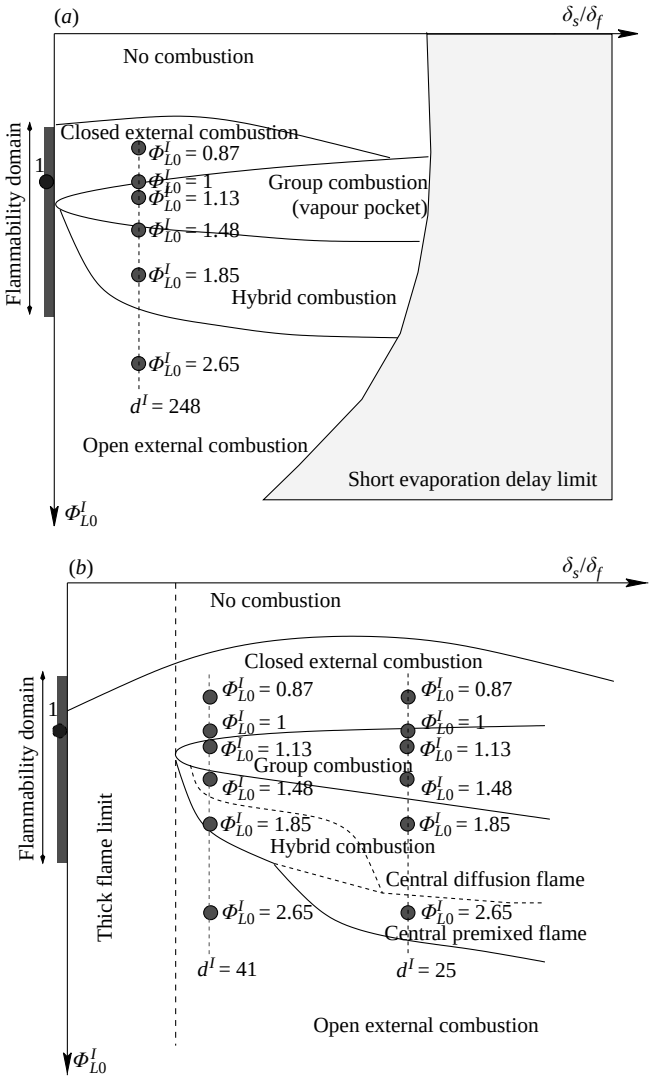


FIGURE 21. Two-dimensional diagrams for diluted spray combustion. Horizontal planes ($\tau_v/\tau_f = \text{const.}$) of the three-dimensionnal diagram proposed in figure 22. (*a*) Short evaporation delay. (*b*) Large evaporation delay.

densities, $d^I = 41$ and $d^I = 25$. Within the 'hybrid' combustion regime, two specific flame structures, issuing from the droplets that have been flushed away from the carrying oxidizer stream, may be observed (figure 15) with either central diffusion flames ($d^I = 41, \Phi_{L0} = 1.48$) or even, for richer mixtures, central premixed flames ($d^I = 25, \Phi_{L0} = 2.65$).

For ($\tau_v/\tau_f > 1$), some droplets may cross the flame front and carry liquid fuel downstream of the reaction zones. Such droplets are generally too heavy for efficient DNS simulations (too sparse droplets). An attempt is made in figure 22 to draw a three-dimensional combustion diagram by a continuation of these two-dimensional diagrams.

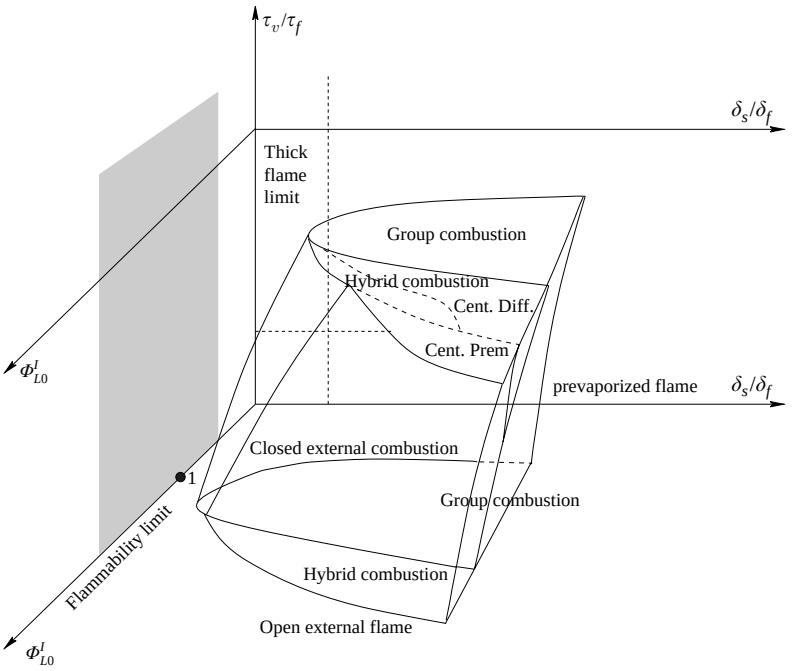


FIGURE 22. Three-dimensional diagram for diluted spray combustion.

## 6. Summary

Direct numerical simulation of the gaseous phase of a spray-jet flame is discussed when the behaviour of the discrete liquid phase is modelled using a Lagrangian description of the evaporating spray with a two-way coupling between the spray and the flow. To guide the analysis, laminar simulations of a flame propagating on a train of droplets in a flow at rest are first examined. Various flame structures are found depending on the fuel/air equivalence ratio within the core of the spray, with a major contribution from partially premixed combustion. Then, forced spray-jet flames are simulated and a large number of flame structures are obtained. An attempt is made to classify those structures into a three-dimensional spray combustion diagram, where the injected spray topology and flame parameters are found to play essential roles.

Because of the large number of parameters involved in spray-jet flames, this classification is somewhat arbitrary, but it helps to distinguish between possible flame structures. Specifically, it shows that varying the properties of an atomizer will strongly modify the structure of the flame base where combustion starts.

CPU time was provided by IDRIS-CNRS (Institut du Développement et des Ressources en Informatique Scientifique). This work was funded by "COS", the French Comity for the development of Supersonic Flight ("Comité d'Orientation Supersonique, Ministère chargé de la Recherche et de la Technologie").

## REFERENCES

BORGHI, R. 1996*a* Background on droplets and sprays. In *Combustion and Turbulence in Two-phase Flows*. Lecture series 1996-02. Von Karman Institute for Fluid Dynamics.

BORGHI, R. 1996*b* The links between turbulent combustion and spray combustion and their modelling. In *Transport Phenomena in Combustion* (ed. S. H. Chang), pp. 1–18. Taylor and Francis.

Borghi, R. & Champion, M. (Eds.) 2000 *Modélisation et Théorie des Flammes*. Technip.

Boulanger, J., Vervisch, L., Réveillon, J. & Ghosal, S. 2003 Effects of heat release in laminar diffusion flames lifted on round jets. *Combust. Flame* **134**, 255–368.

Calimez, X. 1998 Simulation à petite échelle par une méthode vof d'écoulement diphasiques réactifs. PhD thesis, Ecole Centrale Paris.

Candel, S., Lacas, F., Darabiha, N. & Rolon, C. 1999 Group combustion in spray flames. *Multiphase Sci. Tech.* **11**, 1–18.

Cessou, A. & Stepowski, D. 1996 Planar laser induced fluorescence measurement of [oh] in the stabilization stage of a spray jet flame. *Combust. Sci. Tech.* **118**, 361–381.

Chang, S. H. (Ed.) 1996 *Transport Phenomena in Combustion*. Taylor and Francis.

Chigier, N. 1983 Group combustion models and laser diagnostic methods in sprays: a review. *Combust. Flame* **51**, 127–139.

Chiu, H. & Liu, T. 1977 Group combustion of liquid droplets. *Combust. Sci. Technol.* **17**, 127–131.

Chiu, H. H. & Croke, E. J. 1981 Group combustion of liquid fuel sprays. *Energy Technology Lab Rep.* 81-2. University of Illinois at Chicago.

Chiu, H. H., Kim, H. Y. & Croke, E. J. 1982 Internal group combustion of liquid droplets. In *Proc. Nineteenth Symp. (Intl) on Combustion*. The Combustion Institute.

Crowe, C., Sommerfeld, M. & Tsuji, Y. (Eds.) 1998 *Multiphase Flows with Droplets and Particles*. CRC Press.

Elgobashi, S. & Truesdell, G. 1992 Direct numerical simulation of particle dispersion in a decaying isotropic turbulence. *J. Fluid Mech.* **242**, 655–700.

Faeth, G. 1983 Evaporation and combustion of sprays. *Prog. Energy Combust. Sci.* **9**, 1–76.

Givi, P. 1989 Model free simulations of turbulent reactive flows. *Prog. Energy Combust. Sci.* **15**, 1–107.

Kerstein, A. R. & Law, C. K. 1982 Percolation in combustion sprays i: Transition from cluster combustion to percolate combustion in non-premixed sprays. In *Proc. Nineteenth Symp. (Intl) on Combustion*. The Combustion Institute.

Kuo, K. (Ed.) 1986 *Principles of Combustion*. John Wiley and Sons.

Lee, S., Lele, K. & Moin, P. 1991 Numerical simulations of spatially evolving compressible turbulence. *Center for Turbulence Research, Annual Research Briefs*, 126, Stanford.

Lele, S. K. 1992 Compact finite difference schemes with spectral like resolution. *J. Comput. Phys.* **103**, 16–42.

Linán, A. & Williams, F. 1993 *Fundamentals Aspects of Combustion*. Oxford University Press.

Ling, W., Chung, J., Troutt, T. & Crowe, C. 1998 Direct numerical simulation of a three-dimensional temporal mixing layer with particle dispersion. *J. Fluid Mech.* **358**, 61–85.

Mashayek, F. 1998 Direct numerical simulations of evaporating droplet dispersion in forced low mach number turbulence. *Intl J. Heat Mass Transfer* **41**, 2601–2617.

Mashayek, F. 1999 Simulations of reacting droplets dispersed in isotropic turbulence. *AIAA J.* **37**, 1420–1425.

Mashayek, F. 2000 Numerical investigation of reacting droplets in homogeneous shear turbulence. *J. Fluid Mech.* **405**, 1–36.

Mastorakos, E., Baritaud, T. A. & Poinsot, T. J. 1997 Numerical simulations of autoignition in turbulent mixing flows. *Combust. Flame* **109**, 198–223.

Miller, R. & Bellan, J. 1999 Direct numerical simulation of a confined three-dimensional gas mixing layer with one evaporating hydrocarbon-droplet-laden stream. *J. Fluid Mech.* **384**, 293–338.

Miller, R. & Bellan, J. 2000 Direct numerical simulation and subgrid analysis of a transitional droplet laden mixing layer. *Phys. Fluid* **12**, 650–671.

Pantano, C., Sarkar, S. & Williams, F. 2003 Mixing of a conserved scalar in a turbulent reacting shear layer. *J. Fluid Mech.* **481**, 291–328.

Peters, N. 2000 *Turbulent Combustion*. Cambridge University Press.

Poinsot, T., Candel, S. & Trouvé, A. 1996 Direct numerical simulation of premixed turbulent combustion. *Prog. Energy Combust. Sci.* **12**, 531–576.

Poinsot, T. & Lele, S. K. 1992 Boundary conditions for direct simulations of compressible viscous flows. *J. Comput. Phys.* **104**, 104–129.

Poinsot, T. & Veynante, D. 2001 *Theoretical and Numerical Combustion*. Edwards.

Réveillon, J. & Vervisch, L. 2000 Accounting for spray vaporization in non-premixed turbulent combustion modeling: A single droplet model (sdm). *Combust. Flame* **121**, 75–90.

Rogallo, R. S. 1981 Numerical experiments in homogeneous turbulence. *NASA Tech. Mem.* 81315.

Ruetsch, G., Vervisch, L. & Liñán, A. 1995 Effects of heat release on triple flame. *Phys. Fluids* **6**, 1447–1454.

Shirolkar, J., Coimbra, C. F. M. & McQuay, M. Q. 1996 Fundamental aspects of modeling tubulent particle dispersion in dilute flow. *Prog. Energy Combust. Sci.* **22**, 363–399.

Suzuki, T. & Chiu, H. 1971 Multi droplet combustion on liquid propellants. In *Proc. Ninth Intl Symp. on Space and Technology and Science*, pp. 145–154. AGNE, Tokyo, Japan.

Vervisch, L., Labegorre, B. & Réveillon, J. 2004 Hydrogen-sulfur oxy-flame analysis and single-step flame tabulated chemistry. *Fuel* **83**, 605–614.

Vervisch, L. & Poinsot, T. 1998 Direct numerical simulation of non-premixed turbulent flame. *Annu. Rev. Fluid Mech.* **30**, 655–692.

Wray, A. A. 1990 Minimal storage time-advancement schemes for spectral methods. *Center for Turbulence Research Report*. Stanford University.

Yakhot, A., Orszag, S., Yakhot, V. & Israely, M. 1986 Renormalization group formulation of large-eddy simulation. *J. Sci. Comput.* **4**, 139–158.